

SUPPORTING INFORMATION

Computational Screening of Nanoporous Materials for Hexane and Heptane Isomer Separation

Yongchul G. Chung^{1,2‡}, Peng Bai^{3‡}, Maciej Haranczyk⁴, Karson T. Leperi¹, Peng Li⁵, Hongda Zhang¹, Timothy C. Wang⁵, Tim Duerinck¹, Fengqi You⁶, Joseph T. Hupp^{5,7}, Omar K. Farha^{5,8}, J. Ilja Siepmann^{3,9*}, and Randall Q. Snurr^{1*}

¹Department of Chemical and Biological Engineering, Northwestern University, Evanston, IL 60208, United States

²School of Chemical and Biomolecular Engineering, Pusan National University, Busan, South Korea

³Department of Chemical Engineering and Materials Science, University of Minnesota, 421 Washington Avenue SE, Minneapolis, MN 55455, United States

⁴Computational Research Division, Lawrence Berkeley National Laboratory, One Cyclotron Road, MS 50F-1650, Berkeley, CA 94720, United States

⁵Department of Chemistry, Northwestern University, Evanston, IL 60208, United States

⁶Robert Frederick Smith School of Chemical and Biomolecular Engineering, Cornell University, Ithaca, NY 14853, United States

⁷Materials Science Division, Argonne National Laboratory, 9700 S. Cass Avenue, Argonne, IL 60439, United States

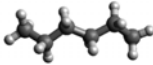
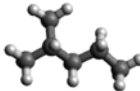
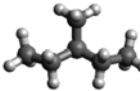
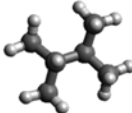
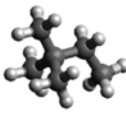
⁸Department of Chemistry, Faculty of Science, King Abdulaziz University, Jeddah 22254, Saudi Arabia

⁹Department of Chemistry and Chemical Theory Center, University of Minnesota, 207 Pleasant Street SE, Minneapolis, MN 55455, United States

Section	Table of Contents	Page Number
S1	Physical and Chemical Properties of Hexane Isomers	pg. 2
S2	Dual-site Langmuir Model Parameters for CoRE MOFs and IZA Zeolites Used for IAST Calculations	pg. 3
S3	Details of Breakthrough Simulations	pg. 5
S4	Discrepancies between S_{L+M} and S_{L+M}^{Henry}	pg. 6 – 9
S5	Discrepancies between S_{L+M} and S_{L+M}^{IAST}	pg. 10
S6	CoRE MOFs and Zeolites with Size-Exclusion for Di-branched Isomers	pg. 11 – 12
S7	High-performing CoRE MOFs Without Reported Gas Sorption Data	pg. 13
S8	Sensitivity Tests for Breakthrough Simulations	pg. 14 – 22
S9	Synthesis, Activation, and Adsorption Measurement of DEYVUA	pg. 23
S10	N ₂ and 3MP Measurements in DEYVUA	pg. 24 – 25
S11	Analysis of Geometric Confinement in VICDOC (Fe ₂ (BDP) ₃)	pg. 26 – 28
S12	Analysis of Free Energy of Adsorption for Hexane Isomer Separation	pg. 29 – 31
S13	DEYVUA	pg. 32 – 35
S14	Effect of Solvent Molecule Evacuation on Adsorption Properties in VICDOC	pg. 36 – 38
S15	Additional Potential Energy Surface and Density Plots	pg. 39 – 40

S1. Physical and Chemical Properties of Hexane Isomers

Table S1. Experimental Physical and Chemical Properties of Hexane Isomers. Critical temperatures and pressure data are obtained from NIST Chemistry WebBook.¹ Kinetic diameters are obtained from Li et al.² RON values are obtained from Ghosh et al.³

Molecule	IUPAC Name	Critical Temperature (K)	Critical Pressure (MPa)	Kinetic Diameter (Å)	Research Octane Number (RON)
	<i>n</i> -hexane	507.6 +/- 0.5	3.02 +/- 0.04	4.3	24.8
	2-methylpentane	497.8 +/- 0.5	3.035 +/- 0.007	5.0	76.0
	3-methylpentane	504.0 +/- 4.0	3.11 +/- 0.06	5.0	76.0
	2,3-dimethylbutane	500.1 +/- 0.5	3.15 +/- 0.08	5.6	105.8
	2,2-dimethylbutane	489.0 +/- 0.5	3.10 +/- 0.02	6.2	91.8

S2. Dual-site Langmuir Model Parameters for CoRE MOFs and IZA Zeolites Used for IAST Calculations

The single-component isotherms were fitted by the dual-site Langmuir adsorption equation:

$$q = N_1 \frac{b_1 p}{1 + b_1 p} + N_2 \frac{b_2 p}{1 + b_2 p} \quad \text{Eq. S1}$$

where N_1 and b_1 are the saturation loading and affinity parameter for the first type of adsorption site, and N_2 and b_2 are the saturation loading and affinity parameter for the second type of adsorption site. Then, using these fitting parameters as input, a Matlab routine was created to estimate the mixture adsorption isotherms at 433 K for equimolar 5-component hexane isomer mixture in all 75 structures based on the ideal adsorbed solution theory (IAST)⁴. The Peng-Robinson equation of state was applied to calculate the fugacity coefficients in the gas phase. **Figures S1-S3** compare the mixture isotherms obtained from IAST estimations and from 5-component mixture GCMC simulations for VICDOC (structure not optimized, “as-is”; see **Section S14**), MRE-1, and DEYVUA. IAST and GCMC simulation results generally agree well for linear and mono-branched isomers for the low-pressure limit, but agree less well for di-branched isomers, especially at high-pressure. Data for IAST parameters and single component isotherms for hexane isomers are available in a separate csv file.

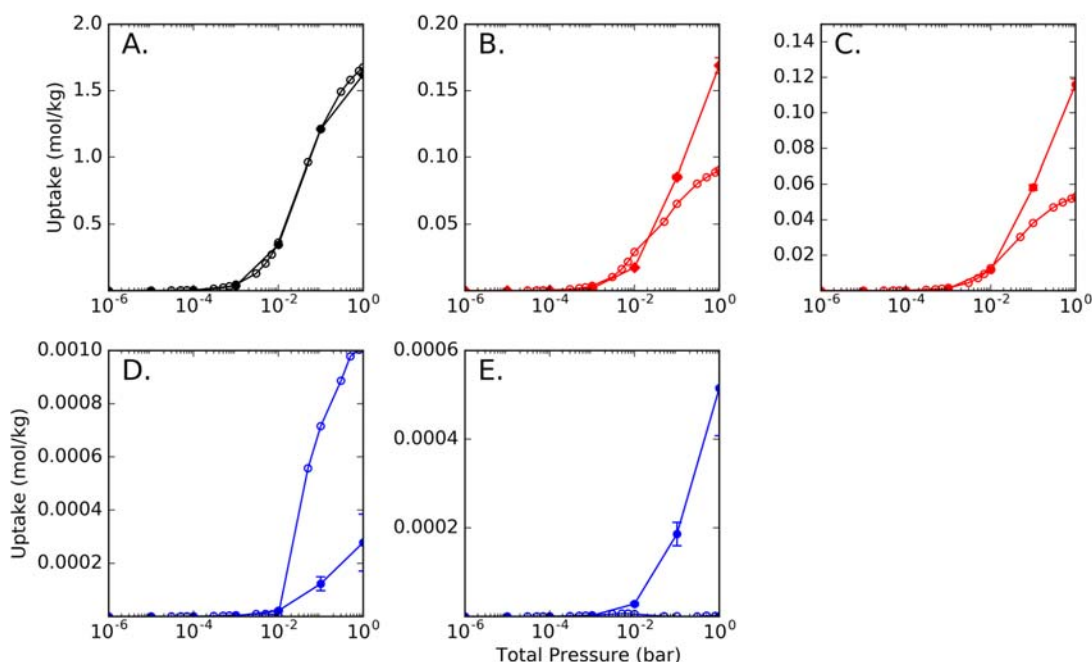


Figure S1. Comparison between IAST estimated (open symbols) and CB-GCMC calculated (filled symbols) 5-component mixture isotherms for VICDOC (“as-is”, see Section S14; $S_{L+M} = 830$, $S_{L+M}^{IAST} = 1180$): **A.** nC6, **B.** 2MP, **C.** 3MP, **D.** 22DMB, **E.** 23DMB. Data points are plotted as a function of total pressure of the system.

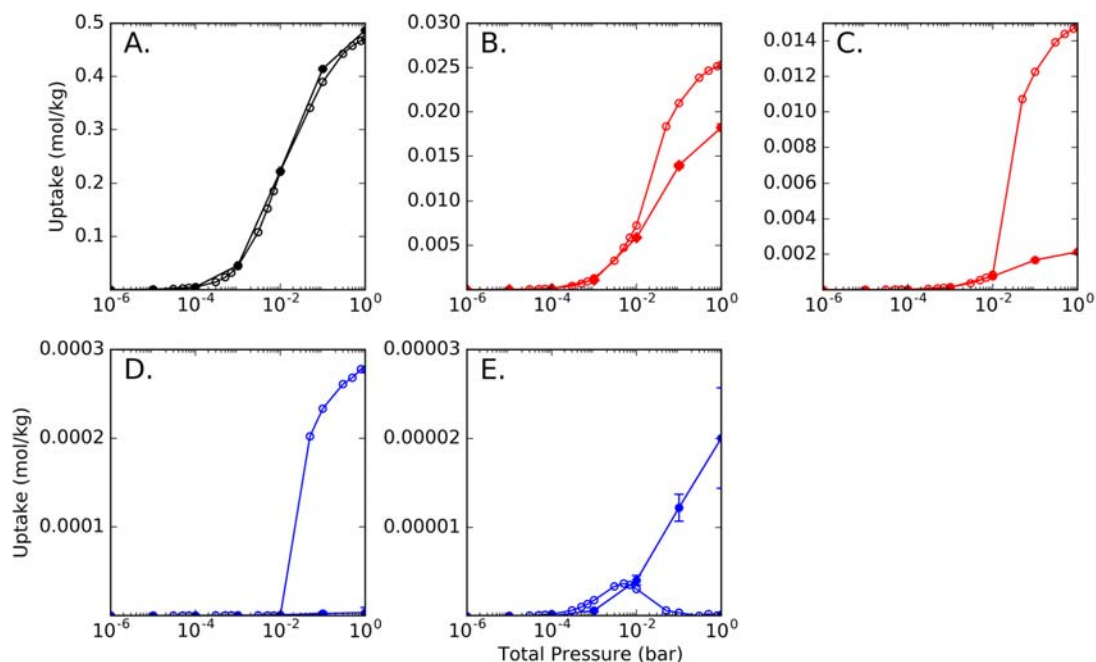


Figure S2. Comparison between IAST estimated (open symbols) and CB-GCMC calculated (filled symbols) 5-component mixture isotherms for MRE-1 ($S_{L+M} = 5200$, $S_{L+M \text{ IAST}} = 1230$): **A.** nC6, **B.** 2MP, **C.** 3MP, **D.** 22DMB, **E.** 23DMB. Data points are plotted as a function of total pressure of the system.

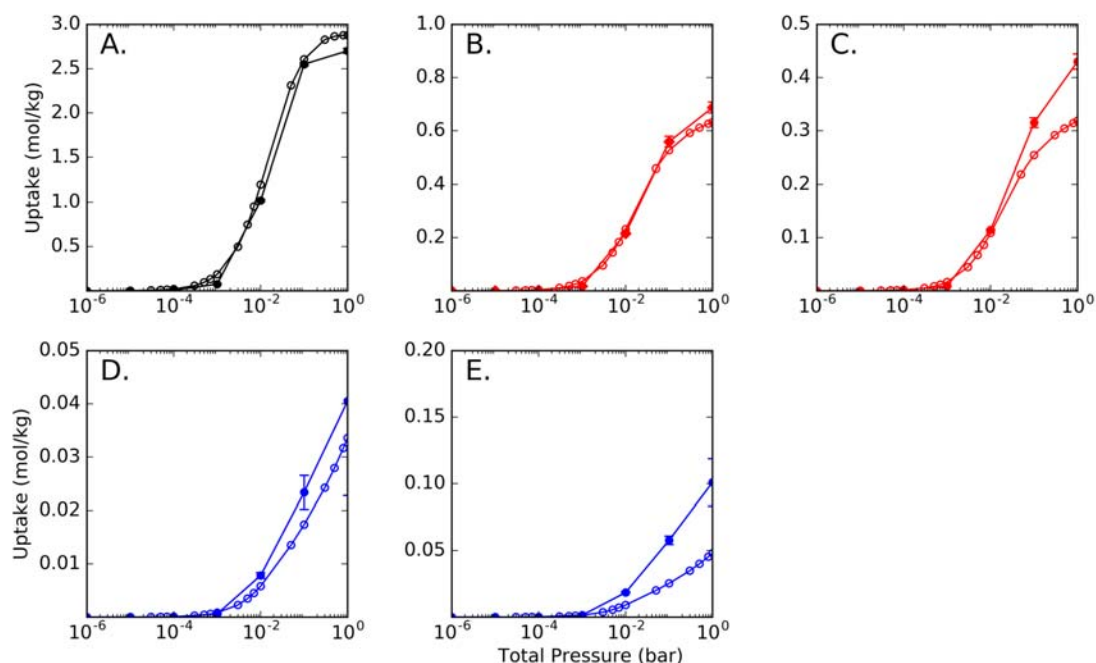


Figure S3. Comparison between IAST estimated (open symbols) and CB-GCMC calculated (filled symbols) 5-component mixture isotherms for DEYVUA ($S_{L+M} = 12$, $S_{L+M \text{ IAST}} = 31$): **A.** nC6, **B.** 2MP, **C.** 3MP, **D.** 22DMB, **E.** 23DMB. Data points are plotted as a function of total pressure of the system.

S3. Details of Breakthrough Simulations

Diffusional effects were considered for the breakthrough simulations using the linear driving force (LDF) model to account for uptake into the MOF. The mass transfer coefficient, k_i for spherical adsorbent pellets was calculated as follows⁵:

$$k_i = 15 \frac{D_{m,i}}{r_c^2} \quad \text{Eq. S2}$$

where $D_{m,i}$ is the intracrystalline diffusion coefficient for component i , and r_c is the crystalline radius. The value of the crystalline radius, r_c , was 500 μm , and a constant value of 15 was used to account for the spherical geometry of the pellets⁶. Here, we assumed that the mass transfer is dominated by intracrystalline diffusion but the mass transfer coefficient is also influenced by the transport to the crystal and through any surface barrier. The diffusion coefficients for the hexane isomers are from the work by Dubbeldam and co-workers⁷ and are given in **Table S2**. We note that the diffusion coefficient for 2,3-dimethylbutane (23DMB) was not available, so the value for 2,2-dimethylbutane (22DMB) was used instead. We also acknowledge that the diffusion coefficients are a material specific parameter and are affected by the loading within the adsorbent material as well. However, for simplicity, we assumed the values of diffusion coefficients among different materials and loading conditions to be the same. For example, n -hexane is assumed to have the same diffusion coefficient ($D = 5 \times 10^{-10} \text{ m}^2/\text{s}$) for VICDOC, DEYVUA, and MRE-1. **Section S8** further discusses the implications of these assumptions. For the breakthrough simulations, a mixture viscosity of $1.0 \times 10^{-5} \text{ Pa}\cdot\text{s}$ was used for calculations of the pressure drop across the column (see equation 6 in the main text).

Table S2: Diffusion coefficients used for the breakthrough simulations.

Hexane Isomers	Diffusion Coefficients (m^2/s)
nC6	5×10^{-10}
2-methylpentane (2MP)	1×10^{-10}
3-methylpentane (3MP)	1×10^{-10}
2,2-dimethylbutane (22DMB)	5×10^{-11}
2,3-dimethylbutane (23DMB)	5×10^{-11}

Table S3: Parameters used for breakthrough simulations

Parameter	Value
Length (L)	0.3 m
Inlet Velocity (v_0)	0.5 m/s
Void Fraction (ϵ)	0.4
Crystal Density (ρ)	1 g/cm ³
Bed Pressure (P_0)	1 bar
Column Temperature (T_0)	433 K

S4. Discrepancies between S_{L+M} and S_{L+M}^{Henry}

Figure 1a from the main text shows discrepancies between the selectivity based on the ratio of Henry's law constants (S_{L+M}^{Henry}) and the selectivity obtained from the GCMC mixture simulations at $p = 1$ bar (S_{L+M}). Out of 318 MOF structures considered, 31 CoRE MOF structures exhibit more than an order of magnitude difference between these two quantities. We consider here two possible contributing factors behind the discrepancies:

- Adsorbate-adsorbate interactions, which are not considered during the Henry's constant calculations, could dominate at the state point of interest (1 bar and 433 K) because of pores with large cavity diameter (LCD > 10 Å).
- There could be different ranges of the Henry's law regime for different adsorbate molecules.

Adsorbate-Adsorbate Interactions

The ratio of S_{L+M} to S_{L+M}^{Henry} was plotted against the adsorbate/adsorbate energy contribution to the total potential energy of the system obtained from the mixture CB-GCMC simulations at $T = 433$ K and $P_{tot} = 1$ bar (**Figure S4**). The results show that the adsorbate-adsorbate interactions can reach as high as 30% of the total energy as the size of the pore becomes larger; this energetic contribution cannot be accounted for in the Henry's constant calculations and leads to the discrepancies between the two selectivities for large-pore MOFs (LCD > 10 Å).

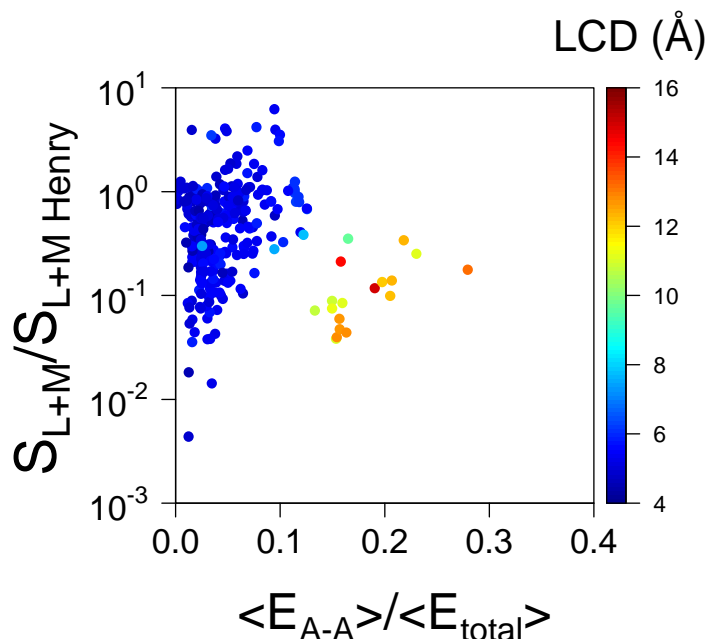


Figure S4. The ratio of S_{L+M} to S_{L+M}^{Henry} as a function of the percentage of the adsorbate-adsorbate contribution to the total potential energy of the system for 318 CoRE MOFs. $\langle E_{total} \rangle$ is the average potential energy of the system at 1 bar and 433 K under five-component mixture condition. $\langle E_{total} \rangle$ is the sum of $\langle E_{A-A} \rangle$ and $\langle E_{H-A} \rangle$. $\langle E_{A-A} \rangle$ is the average potential energy from adsorbate-adsorbate

interactions and $\langle E_{H-A} \rangle$ is the average potential energy from host-adsorbate interactions. Data points are colored based on the largest cavity diameter (LCD) of the corresponding structure.

Difference in the Henry's Law Regime for Different Isomers

The Henry's law regime is defined as the initial pressure range in the isotherm, which exhibits a linear increase in gas adsorption with increasing pressure. In Figures S5 and S6, we plot the comparison between single-component isotherms predicted from the Henry's law constant and single-component isotherms obtained from GCMC simulation for two MOFs. The results show that deviations from the Henry's law regime become significant for *n*-hexane at $p \approx 10^{-4}$ bar (10^1 Pa), and for mono-branched isomers $p \approx 10^{-3}$ bar (10^2 Pa), whereas the Henry's law regime for di-branched isomers extends to $p \approx 0.1$ bar. This quantitative difference can be assessed by examining the difference in the pressure (P_{Henry}) at which the Henry's law regime is no longer valid for a given isomer. For simplicity, P_{Henry} is defined here as the value at which the ratio between isomer loading from GCMC simulation and the isomer loading based on the Henry's law constant becomes less than 1/10. For example, P_{Henry} value for *n*-hexane is 10^2 Pa for OHAKIS because at this pressure, *n*-hexane uptake from GCMC simulation is ~ 1.0 mol/kg and *n*-hexane uptake predicted from Henry's law constant is >10 mol/kg. The results are tabulated in Table S4. P_{Henry} values for the structures with large percentage of adsorbate-adsorbate interaction energy ($>10\%$) are similar to one another, which indicates that adsorbate-adsorbate interactions are the main source of discrepancies in these structures. For the structures where adsorbate-adsorbate interaction energy is less than 10 %, we observe large differences among P_{Henry} for different hexane isomers, suggesting that the difference in P_{Henry} is the key source of the discrepancies between S_{L+M} and S_{L+M}^{Henry} among these structures.

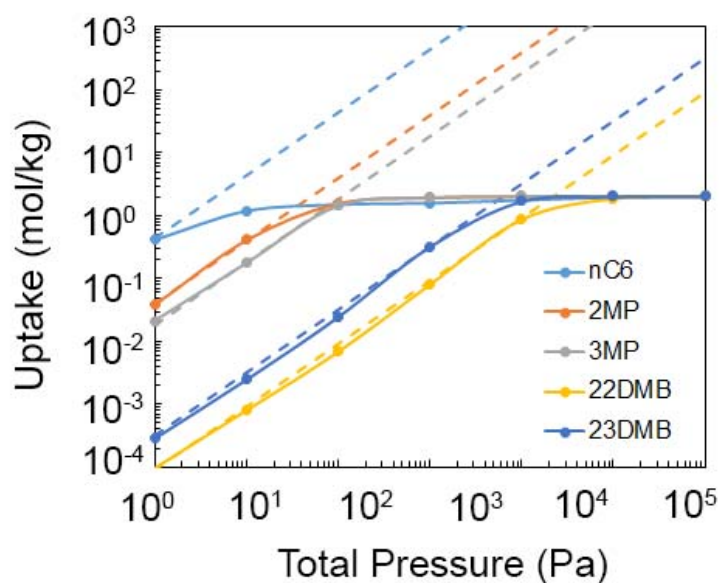


Figure S5. Henry's law constant prediction of hexane isomer uptake (dotted lines) and GCMC single component isotherms (solid lines) for OHAKIS ($S_{L+M} = 38$ and $S_{L+M, Henry} = 813$). The values of P_{Henry} are different for nC6 ($\sim 10^2$), 2MP ($\sim 10^3$), 3MP ($\sim 10^3$), 22DMB ($\sim 10^5$) and 23DMB ($\sim 10^6$).

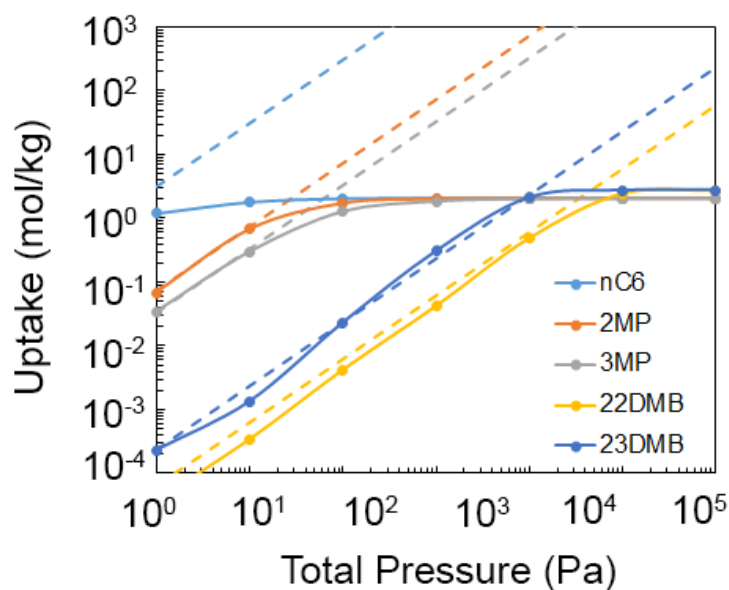


Figure S6. Henry's law constant prediction of hexane isomer uptake (dotted lines) and GCMC single component isotherms (solid lines) for QOZDOY ($S_{L+M} = 102$ and $S_{L+M, Henry} = 7,127$). P_{Henry} values are different for nC6 ($\sim 10^0$), 2MP ($\sim 10^2$), 3MP ($\sim 10^2$), 22DMB ($\sim 10^4$), and 23DMB ($\sim 10^5$).

Table S4. Summary of discrepancies between S_{L+M} and $S_{L+M \text{ Henry}}$. The structures listed here are the ones with large deviation in Henry selectivity ($S_{L+M \text{ Henry}}$) and finite-loading selectivity from GCMC simulations (S_{L+M}). Materials are listed from the ones with the largest percentage of adsorbate-adsorbate interaction energy to the ones with smallest percentage of adsorbate-adsorbate interaction energy during 5-component equimolar mixture GCMC simulation at 1 bar and 433 K. The structures shown in **Figures S5** and **6** are highlighted in blue.

REFCODE	Percentage of Adsorbate- Adsorbate Interaction Energy	P_{Henry} (Pa)				
		nC6	2MP	3MP	23DMB	22DMB
PAMTOO	25.6 %	10^4	10^4	10^4	10^4	10^4
CUVHIL02	19.5 %	10^6	10^6	10^6	10^6	10^6
AMIMEP	18.9 %	10^4	10^4	10^4	10^4	10^4
CUVHEH	18.6 %	10^6	10^6	10^6	10^6	10^6
CUVHIL01	18.6 %	10^6	10^6	10^6	10^6	10^6
CUVHIL	18.2 %	10^6	10^6	10^6	10^6	10^6
AMIMAL	18.1 %	10^4	10^4	10^4	10^4	10^4
AMILOY	17.6 %	10^2	10^4	10^4	10^4	10^4
AMILUE	17.6 %	10^1	10^4	10^4	10^4	10^4
AWEJIW	15.4 %	10^3	10^4	10^4	10^5	10^5
HEKTAU	6.8 %	10^4	10^4	10^4	10^4	10^5
OSAWEL	4.7 %	10^1	10^2	10^2	10^3	10^4
GAYGAQ	4.1 %	10^3	10^3	10^3	10^5	10^5
OHAKIS	3.9 %	10^2	10^3	10^3	10^5	10^6
QOZDOY	3.6 %	10^0	10^2	10^2	10^4	10^5
IXISAJ	3.4 %	10^1	10^2	10^3	10^4	10^4
RASKIH	3.4 %	10^1	10^2	10^2	10^4	10^5
ILIFUE	3.3 %	10^3	10^3	10^4	10^5	10^5
ILIGAL	3.1 %	10^3	10^4	10^5	10^6	10^6
ILIGEP	3.1 %	10^3	10^4	10^5	10^6	10^6
IXISOX	3.0 %	10^2	10^3	10^3	10^4	10^4
LEDHIN	2.5 %	10^2	10^3	10^4	10^5	10^6
OKIVIO	2.5 %	10^2	10^3	10^3	10^4	10^5
ITIWIS	2.4 %	10^2	10^3	10^4	10^5	10^6
EDAVOV	1.9 %	10^3	10^3	10^3	10^4	10^4
CADPII	1.6 %	10^2	10^3	10^4	10^5	10^5
KEYFIF	1.6 %	10^3	10^4	10^5	10^5	10^6
IBUDOZ	1.5 %	10^4	10^6	10^6	10^6	10^6
XEJVOZ	1.4 %	10^1	10^2	10^3	10^5	10^4
TONBII	1.3 %	10^0	10^3	10^4	10^6	10^6
KEYFIF01	1.2 %	10^3	10^4	10^5	10^5	10^6

S5. Discrepancies between S_{L+M} and S_{L+M}^{IAST}

Figure 1b shows some structures with relatively large differences between S_{L+M} and S_{L+M}^{IAST} . In some cases, the large difference can be attributed to inaccurate estimation of the saturation loadings (N_1 and N_2 parameters) of hexane isomers in the Langmuir model, which were evaluated at 100 bar (10^7 Pa). As shown in **Figure S7**, for some materials the isotherms of the di-branched isomers have not plateaued at 100 bar, leading to an error in the estimate of the saturation loadings. The values of N_1 and N_2 are used as inputs to the IAST calculations, so any errors in these values may lead to errors in the IAST predictions of S_{L+M}^{IAST} .

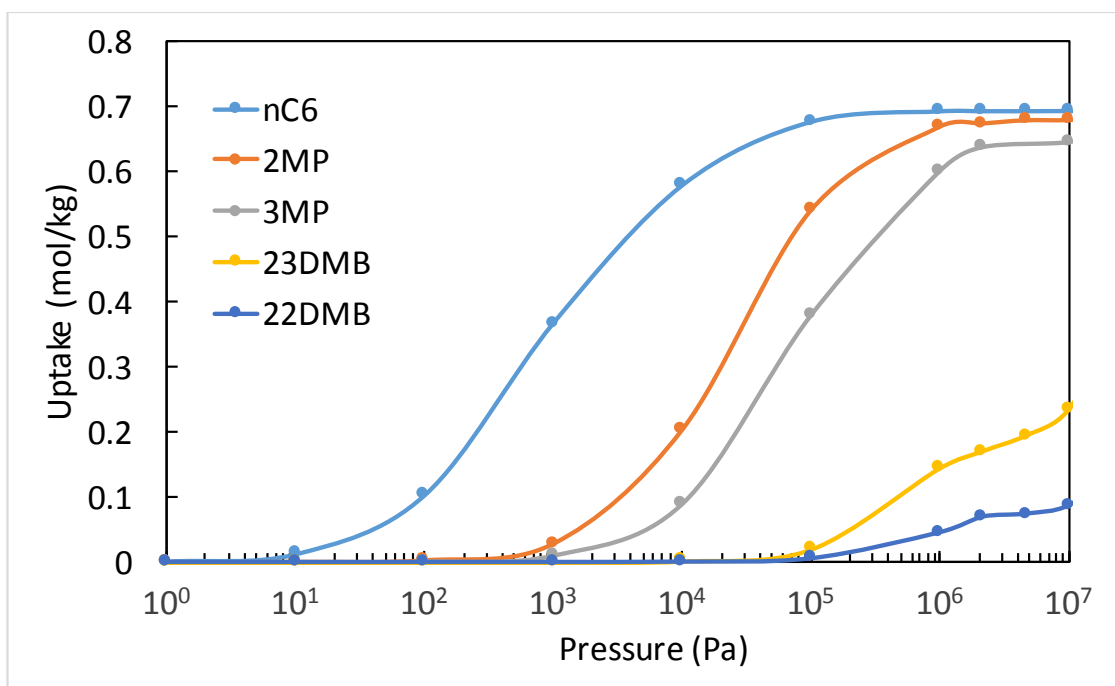


Figure S7. Single-component isotherms for hexane isomers in CAN-1 at 433 K.

S6. CoRE MOFs and Zeolites with Size-Exclusion for Di-branched Isomers

Table S5. Data for linear and mono-branched hexane isomer uptake of CoRE MOFs that do not adsorb 22DMB and 23DMB at 1 bar and 433 K under equimolar 5-component mixture condition.

REFCODE	nC6 (mol/kg)	2MP (mol/kg)	3MP (mol/kg)	22DMB (mol/kg)	23DMB (mol/kg)	Total Uptake (mol/kg)	Percentage of nC6 Uptake
BEDHOJ	1.96867	0	0	0	0	1.96867	100.0
CAYBAH01	0.00064	0.00011	0.00003	0	0	0.00078	82.1
EQUBIC	0.65351	0.00712	0.00374	0	0	0.66437	98.4
FIPWUY	1.70344	0.02169	0.00022	0	0	1.72535	98.7
HEXNII	0.81697	0.00122	0.00012	0	0	0.81831	99.8
HICVOG	1.95176	0.19283	0.02664	0	0	2.17123	89.9
IBUYAH	0.07511	0.00474	0.00013	0	0	0.07998	93.9
ITAHEQ	0.35543	0.00592	0.00129	0	0	0.36264	98.0
IWELIG	0.7131	0	0	0	0	0.7131	100.0
IWELOM	0.73354	0	0	0	0	0.73354	100.0
JILXOS	0.64579	0.00052	0.00008	0	0	0.64639	99.9
KANCIN	1.16949	0.01073	0.00663	0	0	1.18685	98.5
LIFWOO	2.12769	0.1009	0.0223	0	0	2.25089	94.5
LUFQUZ02	1.25102	0.00089	0	0	0	1.25191	99.9
MABKEG	0.82745	0.03341	0.00761	0	0	0.86847	95.3
MIMVEJ	1.93805	0	0	0	0	1.93805	100.0
NADZEZ	1.37165	0.00572	0.00181	0	0	1.37918	99.5
NICJOA	0.34766	0.00015	0.00009	0	0	0.3479	99.9
ODOXEK	0.378	0.0044	0.00013	0	0	0.38253	98.8
OSILOS	0.65735	0.00224	0.00108	0	0	0.66067	99.5
OSIWUJ	0.58542	0	0	0	0	0.58542	100.0
PARMIG	1.96822	0	0	0	0	1.96822	100.0
PAVLUU	1.4922	0.04311	0.00657	0	0	1.54188	96.8
PIHJOH	0.83472	0.00446	0.00326	0	0	0.84244	99.1
PURTEC	0.35242	0	0	0	0	0.35242	100.0
QADBII	0.92857	0.02186	0.00091	0	0	0.95134	97.6
QATPUX	0.81541	0	0	0	0	0.81541	100.0
QEDZEG	0.99845	0.01474	0.00474	0	0	1.01793	98.1
REGJIW02	0.09206	0	0	0	0	0.09206	100.0
RURPEA	0.89926	0.00718	0.00043	0	0	0.90687	99.2
VUHJAK	0.58343	0.00811	0.00133	0	0	0.59287	98.4
WECFAN01	0.29334	0.00082	0.00027	0	0	0.29443	99.6
WOHSIV	0.39317	0.00037	0.00006	0	0	0.3936	99.9
XAYMUF	1.48565	0.22522	0.02019	0	0	1.73106	85.8
XOJWEZ	1.12837	0.04585	0.00549	0	0	1.17971	95.6
ZERQOE	0.59063	0	0	0	0	0.59063	100.0

Table S6. Data for linear and mono-branched hexane isomer uptake of IZA zeolites that do not adsorb 22DMB and 23DMB at 1 bar and 433 K under equimolar 5-component mixture condition.

IZA FTC	nC6 (mol/kg)	2MP (mol/kg)	3MP (mol/kg)	22DMB (mol/kg)	23DMB (mol/kg)	Total Uptake (mol/kg)	Percentage of nC6 Uptake
BOF-0	0.4609	0.0258	0.0007	0	0	0.4874	94.6
WEN-0	0.4064	0.0298	0.0031	0	0	0.4393	92.5
FER-2	0.1442	0.0011	0.0003	0	0	0.1456	99.0
ASV-0	0.0348	0	0	0	0	0.0348	100.0
JSN-1	0.0006	0.0004	0	0	0	0.001	60
MAR-0	0.4288	0.0133	0.0004	0	0	0.4425	96.9
ATO-1	0.5738	0.0099	0.0025	0	0	0.5862	97.9
AFO-1	0.2740	0.0204	0.0015	0	0	0.2959	92.6
PCR-1	0.032	0.0019	0.0001	0	0	0.034	94

S7. Data for High-performing CoRE MOFs without Reported Gas Sorption

In **Table 2** of the main text, we excluded MOFs for which there are no reported gas sorption results. One must approach such materials with some caution, because their stability to evacuation of guest molecules may not have been established. These materials are listed in **Table S7**.

Table S7. Physical properties and equimolar mixture uptake data from GCMC simulation for CoRE MOFs with no reported experimental gas sorption data with $S_{L+M} > 10$ and $q_{L+M} > 0.60$ mol/kg at $p = 1$ bar and $T = 433$ K. q_i is the mixture uptake (mol/kg), where the subscript i denotes the corresponding hexane isomer. PLD is the pore limiting diameter, LCD is the largest cavity diameter, GSA is the gravimetric surface area. GSA is obtained using a sphere probe with $d=3.68$ Å.

REFCODE	PLD (Å)	LCD (Å)	GSA (m ² /g)	q_{nc6}	q_{2mp}	q_{3mp}	q_{22dmb}	q_{23dmb}	S_{L+M}	q_{L+M} (mol/kg)
VEDVUW	4.0	5.1	870	1.089	0.697	0.566	0.133	0.004	336	0.635
DEJCIF	4.6	5.1	685	1.679	0.259	0.097	0.009	0.002	130	0.678
ZEXKUK	4.1	5.4	989	1.670	0.387	0.053	0.015	0.007	106	0.702
QOZDOY	5.1	5.4	2098	2.284	0.912	0.604	0.185	0.051	101	0.686
DEKHEH	4.6	5.4	676	1.384	0.447	0.065	0.057	0.002	66	0.703
SOWYOS	4.0	5.1	888	1.153	0.627	0.554	0.150	0.004	62	0.745
VILXOE	4.2	5.4	978	2.174	0.373	0.107	0.041	0.004	62	0.698
RASKIH	4.7	5.3	696	1.937	0.081	0.042	0.013	0.000	46	0.639
QOMFAA	4.6	5.4	701	1.357	0.352	0.211	0.027	0.000	39	0.884
UWOWAF	4.9	5.2	979	1.333	0.502	0.242	0.130	0.000	32	0.707
EBELUU	4.1	5.4	1650	2.222	0.528	0.417	0.200	0.008	30	0.772
SIQQEO	4.7	5.4	1401	1.618	0.551	0.431	0.031	0.051	21	0.867
SOVHAM	4.2	4.9	941	1.549	0.209	0.184	0.071	0.000	18	0.647
ABUWOJ	4.1	5.5	1303	1.798	0.319	0.120	0.022	0.002	11	0.784
FAHGAY	4.2	5.5	768	1.761	0.247	0.115	0.035	0.009	10	1.267
REJLEY	4.0	5.1	578	1.305	0.562	0.040	0.002	0.002	10	0.693
SERWAP	4.6	5.4	792	1.607	0.409	0.081	0.019	0.004	10	1.055
NAKLIW	4.1	5.4	997	1.765	0.299	0.041	0.008	0.005	10	0.778

S8. Sensitivity Tests for Breakthrough Simulations

A series of breakthrough simulations were carried out with different diffusion coefficients for DEYVUA, VICDOC, and MRE to test the effect of diffusion coefficients on breakthrough characteristics. We considered three different cases:

1. **Case I:** *D values for all hexane isomers are artificially reduced by 1 or 2 orders of magnitude from the base values in Table S2.*
2. **Case II:** *D values for di-branched isomers are artificially set to $D \sim 10^{-12} \text{ m}^2/\text{s}$ or $10^{-13} \text{ m}^2/\text{s}$ while diffusion coefficients for n-hexane and mono-branched hexane isomers are from Table S2.*
3. **Case III:** *Breakthrough is simulated in the absence of diffusional effect (i.e., $D \sim 1 \times 10^{-4} \text{ m}^2/\text{s}$ for all hexane isomers).*

To compare the impact of diffusion coefficients, Research Octane Number (RON) values based on the mole fractions of hexane isomers were calculated as discussed in the main text. The cycle time is defined as the difference between the breakthrough time (t_b), and the time when the RON value of the outlet stream falls below 92. In VICDOC and MRE-1, the value of t_b is less than 2 seconds, since the di-branched isomers breakthrough almost instantaneously. However, in DEYVUA, the value of t_b is in the order of tens of seconds. The longer breakthrough time in DEYVUA compared to other adsorbent is due to the larger capacity for di-branched hexane isomers for this adsorbent material.

Breakthrough Characteristics of DEYVUA

Figure S8 shows the results from **Case I** for DEYVUA. **Figure S8a** shows the results based on the diffusion coefficients listed in **Table S2**. The cycle time for the base case scenario is 471 seconds. **Figure S8b** shows the results when the diffusion coefficients for all hexane isomers are reduced by one order of magnitude compared to the base case. This leads to immediate breakthrough of the mono-branched hexane isomers and a cycle time < 1 second. **Figure S8c** shows the corresponding results when the diffusion coefficients are reduced by two orders of magnitude. In this case, there is immediate breakthrough of all hexane isomers and a cycle time of 0 seconds. In the last scenario, the RON of the outlet stream never reaches above 88.2 because the outlet stream is contaminated by both linear and mono-branched hexane isomers.

Figure S9 shows the results from **Case II** for DEYVUA. When the diffusion coefficients of the di-branched hexane isomers are reduced by an order of magnitude (**Figure S9b**), the di-branched isomers start to breakthrough immediately, which leads to a slight increase in cycle time compared to the *Base Case* ($471 \text{ s} \rightarrow 525 \text{ s}$). Decreasing the diffusion coefficients of the di-branched isomers by two orders of magnitude (**Figure S9c**) has negligible further impact on the breakthrough time, since the di-branched isomers are already breaking through immediately if their diffusion coefficients are reduced by one order of magnitude.

Breakthrough Characteristics of VICDOC

Figure S10 shows the results from **Case I** for VICDOC. **Figure S10a** shows the results based on the diffusion coefficients listed in **Table S2**. The cycle time for the base case scenario is 211 seconds. **Figure S10b** shows the results when the diffusion coefficients for all hexane isomers are reduced by one order of magnitude compared to the base case. This leads to immediate breakthrough of both mono and di-branched isomers, and because of this “contaminated” product stream, the RON value of the product stream never reaches above 89.6. Thus, the cycle time is zero for this

scenario. When the diffusion coefficients are further reduced by another order of magnitude (**Figure S10c**), the RON value of the product stream never reaches above 84.9.

Figure S11 shows the results from **Case II** for VICDOC. As seen for DEYVUA, a decrease in the diffusion coefficients leads to faster breakthrough of hexane isomers. Since the di-branched isomers are already breaking through immediately using the diffusion coefficients from **Table S2**, any further decrease in their diffusion coefficients does not have any impact on the cycle time.

Breakthrough Characteristics of MRE

Figure S12 shows the results from **Case I** for MRE-1. **Figure S12a** shows the results based on the diffusion coefficients listed in **Table S2**. The cycle time for the base case scenario is < 1 second.

Figure S12b shows the results when the diffusion coefficients for all hexane isomers are reduced by one order of magnitude compared to the base case. This leads to immediate breakthrough of all mono-branched and di-branched hexane isomers, and the RON value never reaches above 87.7. When the diffusion coefficients are further reduced by another order of magnitude (**Figure S12c**), the RON value of the product stream never reaches above 82.7.

Figure S13 shows the results from **Case II** for MRE-1. Since the decrease in diffusion coefficient limits the mass transfer of the species into the MOF pores, it will lead to faster breakthrough time. Since di-branched hexane isomers are already breaking through immediately for MRE-1 based on the diffusion coefficients from **Table S2**, any further decrease in their diffusion coefficients does not have any impact on the cycle time.

No Diffusional Effects

To simulate the breakthrough column without diffusional effects, the diffusion coefficients for all components were raised to $1 \times 10^{-4} \text{ m}^2/\text{s}$, which is 6 – 7 orders of magnitude larger than the values from **Table S2**. **Figure S14** compares the breakthrough curves for DEYVUA, VICDOC, and MRE under this scenario. For DEYVUA, the cycle time is reduced from 471 to 40 seconds, which is due to slower initial breakthrough of the di-branched isomers. For VICDOC, the cycle time increases from 211 to 280 seconds without diffusional limitations. For MRE-1, the cycle time increases from 0 to 50 seconds without diffusional limitations. For all cases, the RON curves (**Figure S13e** and **S13f**) become sharper when there are no diffusion limitations.

Based on the sensitivity studies presented here, we emphasize that the values of the diffusion coefficients are important for accurate determination of the breakthrough characteristics and the cycle times (which subsequently affect the operating cost of the separation unit). In particular, we expect the values of the diffusion coefficients to have a large impact for the adsorbent materials with significant mono and di-branched isomer uptake if these species fit very tightly. In such cases, diffusional effects may be an important design variable for the development of new materials for hexane isomer separation. On the other hand, if all molecules diffuse readily (such as **Case III**), then diffusional effects play a secondary role compared to adsorption thermodynamics and may not be relevant.

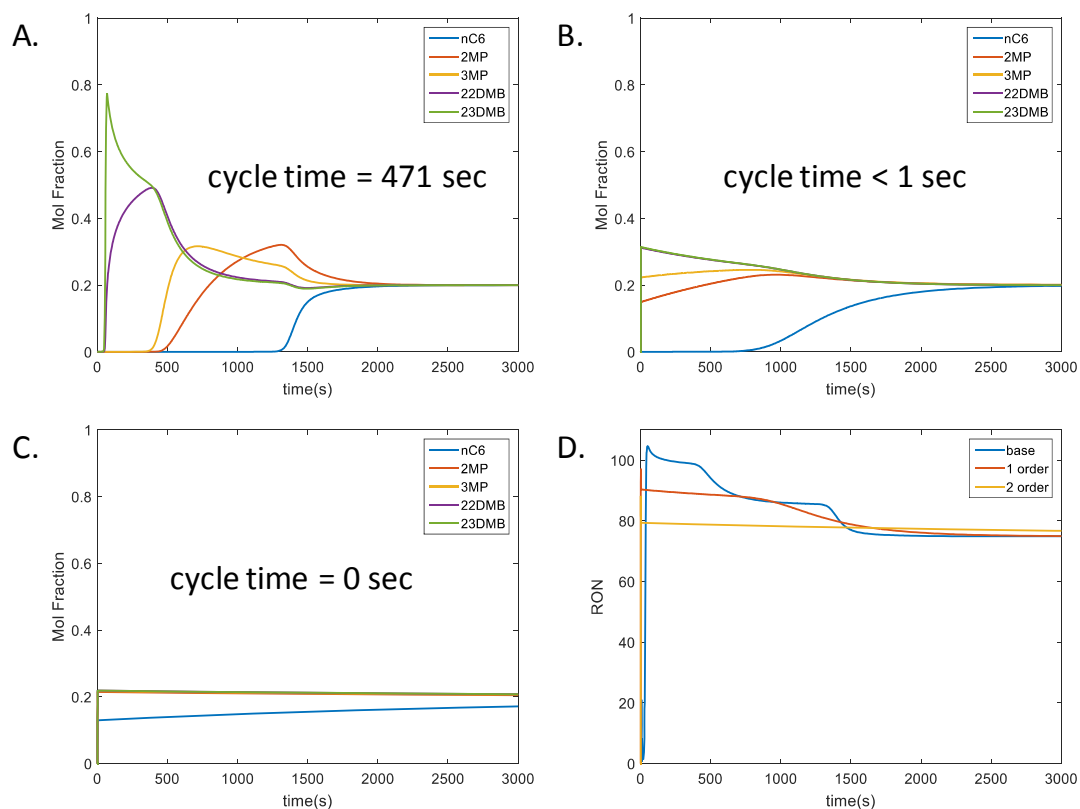


Figure S8: Breakthrough simulation results and RON values for DEYVUA for **Case I**: **A.** *D* values are from **Table S2**, **B.** *D* values from **Table S2** were reduced by 1 order of magnitude. **C.** *D* values from **Table S2** were reduced by 2 orders of magnitude, **D.** RON values from **A**, **B**, and **C**.

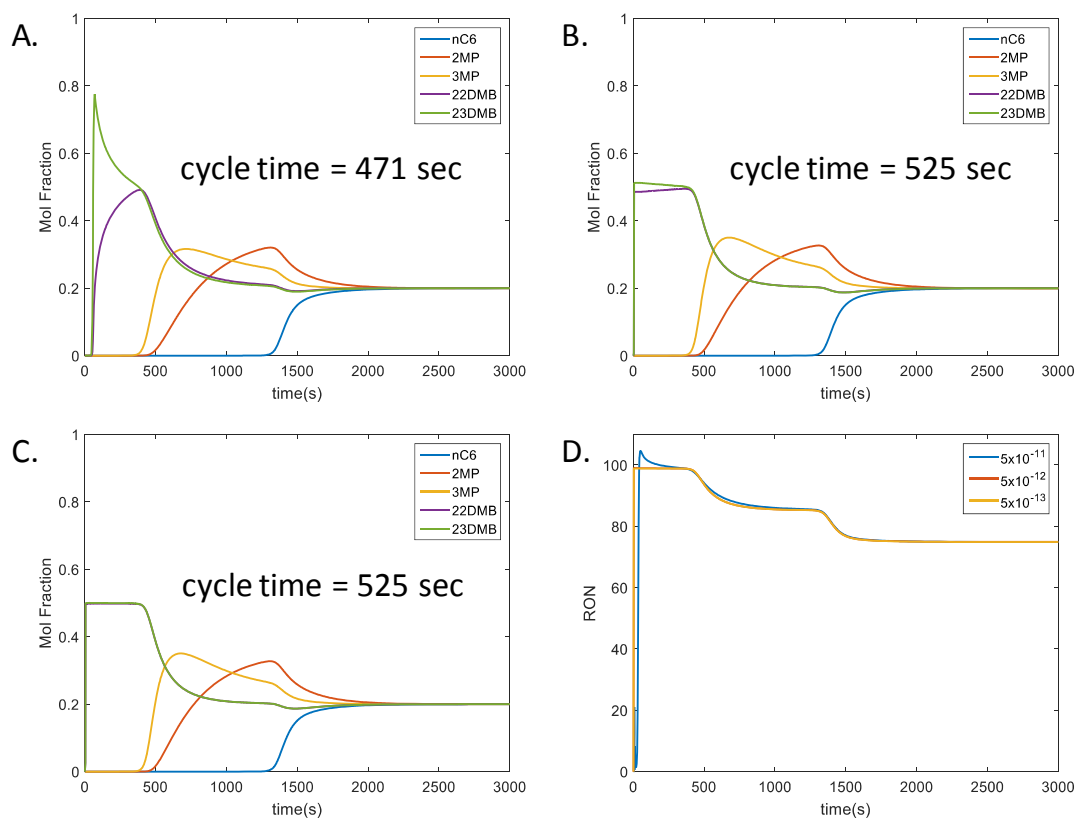


Figure S9: Breakthrough simulation results and RON values for DEYVUA for **Case II**: **A.** *D* values are from Table S2, **B.** *D* values for di-branched isomers were reduced by 1 order of magnitude. **C.** *D* values for di-branched isomers were reduced by 2 orders of magnitude, **D.** RON values from **A**, **B**, and **C**.

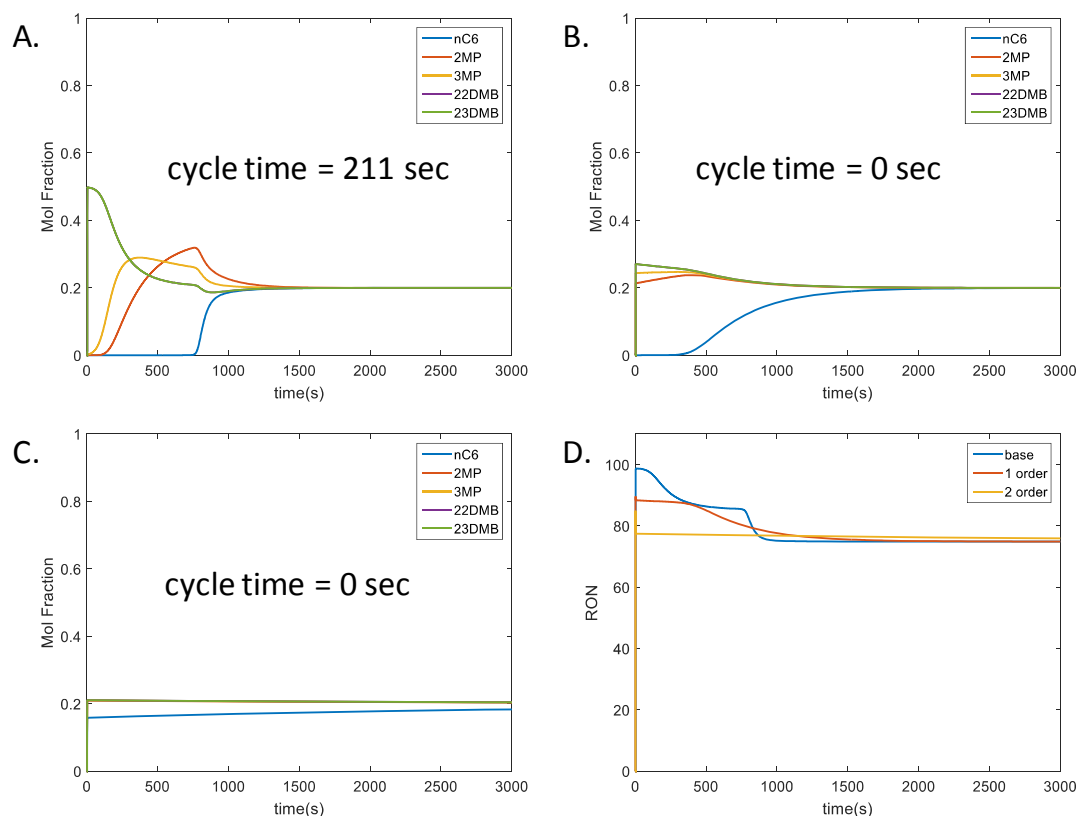


Figure S10: Breakthrough simulation results and RON values for VICDOC for **Case I**: **A.** *D* values are from Table S2, **B.** *D* values from Table S2 were reduced by 1 order of magnitude. **C.** *D* values from Table S2 were reduced by 2 orders of magnitude, **D.** RON values from **A**, **B**, and **C**.

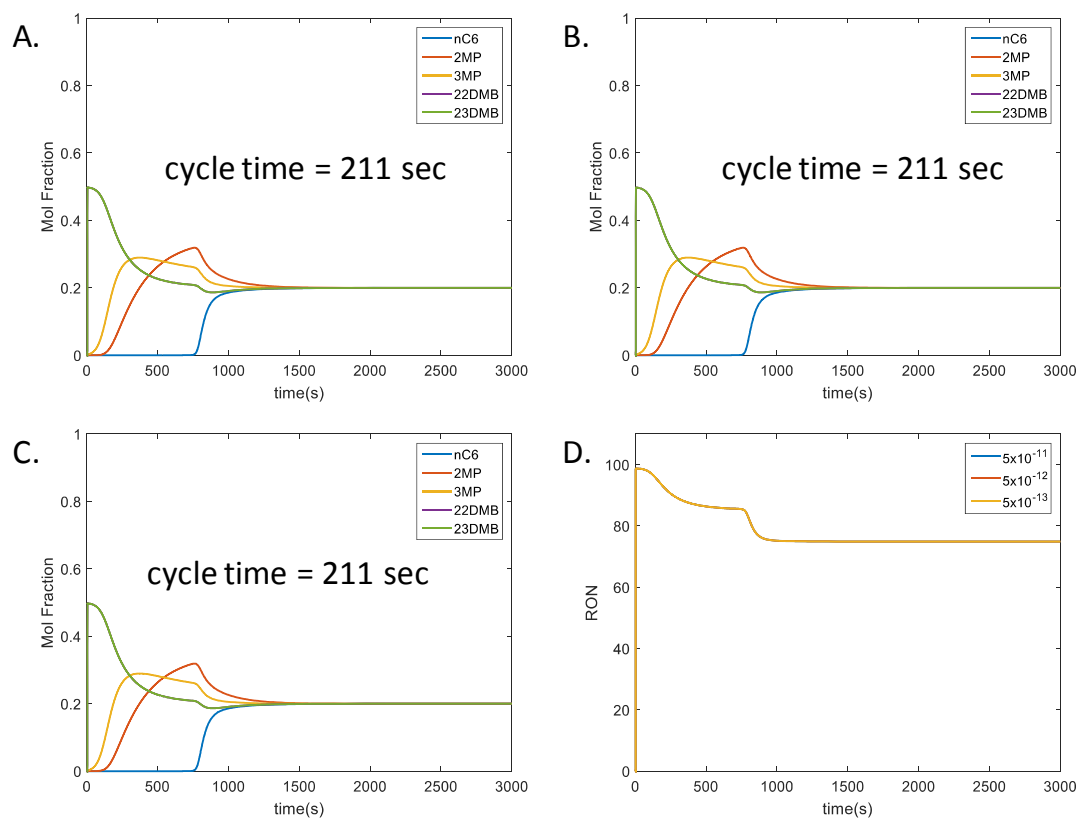


Figure S11: Breakthrough simulation results and RON values for VICDOC for **Case II**: **A.** *D* values from **Table S2**, **B.** *D* values for di-branched isomers were reduced by 1 order of magnitude. **C.** *D* values for di-branched isomers were reduced by 2 orders of magnitude, **D.** RON values from **A**, **B**, and **C**.

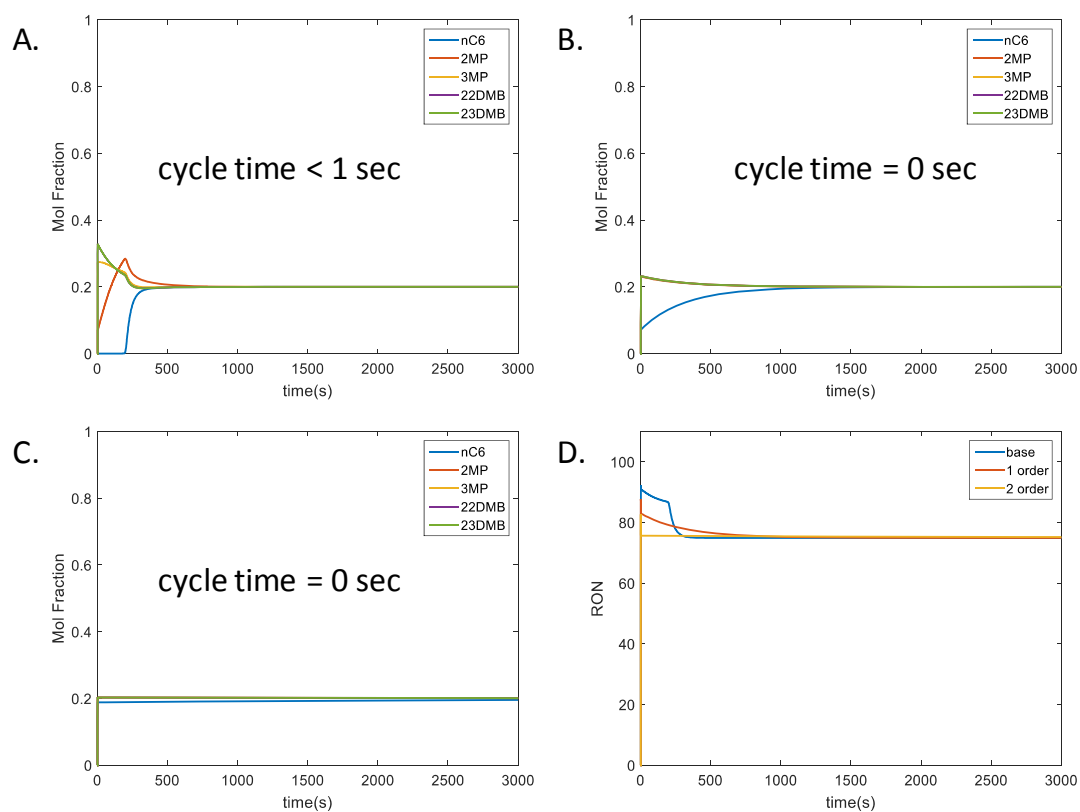


Figure S12: Breakthrough simulation results and RON values for MRE-1 for **Case I**: **A.** *D* values are from **Table S2**, **B.** *D* values from **Table S2** were reduced by 1 order of magnitude, **C.** *D* values from **Table S2** were reduced by 2 orders of magnitude, **D.** RON values from **A**, **B**, and **C**.

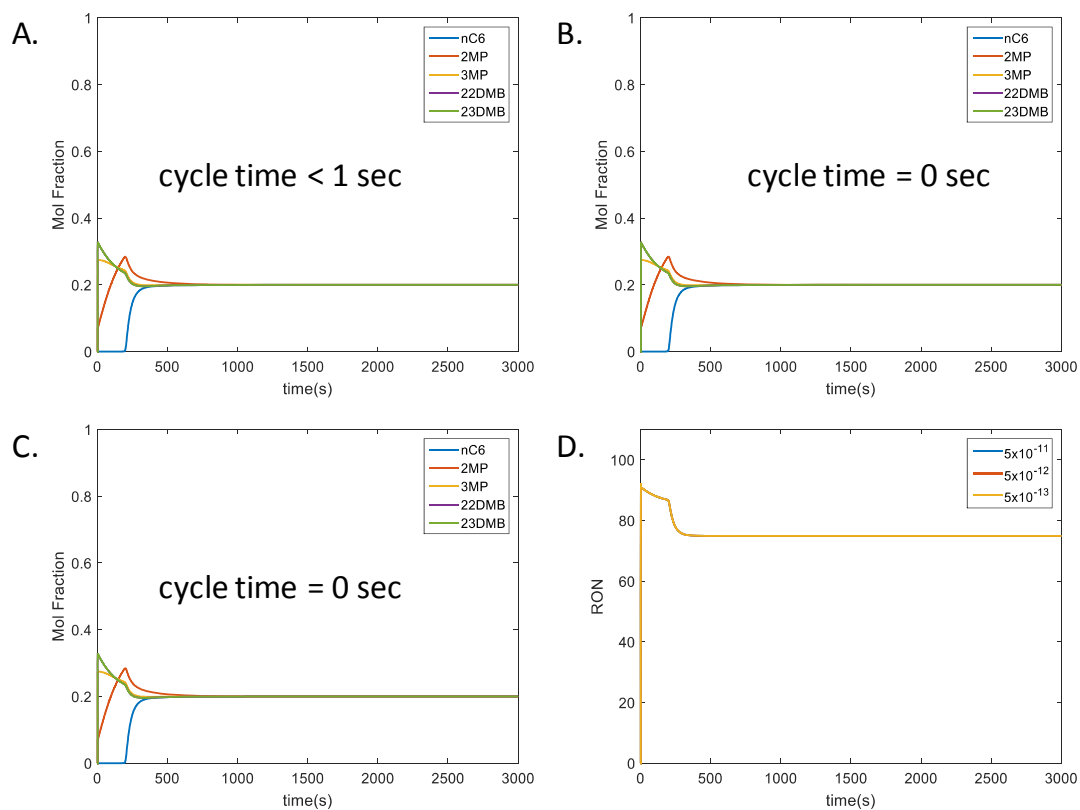


Figure S13: Breakthrough simulation results and RON values for MRE-1 for **Case II**: **A.** D values are from **Table S2**, **B.** D values for di-branched isomers were reduced by 1 order of magnitude, **C.** D values for di-branched isomers were reduced by 2 orders of magnitude, **D.** RON values from **A**, **B**, and **C**.

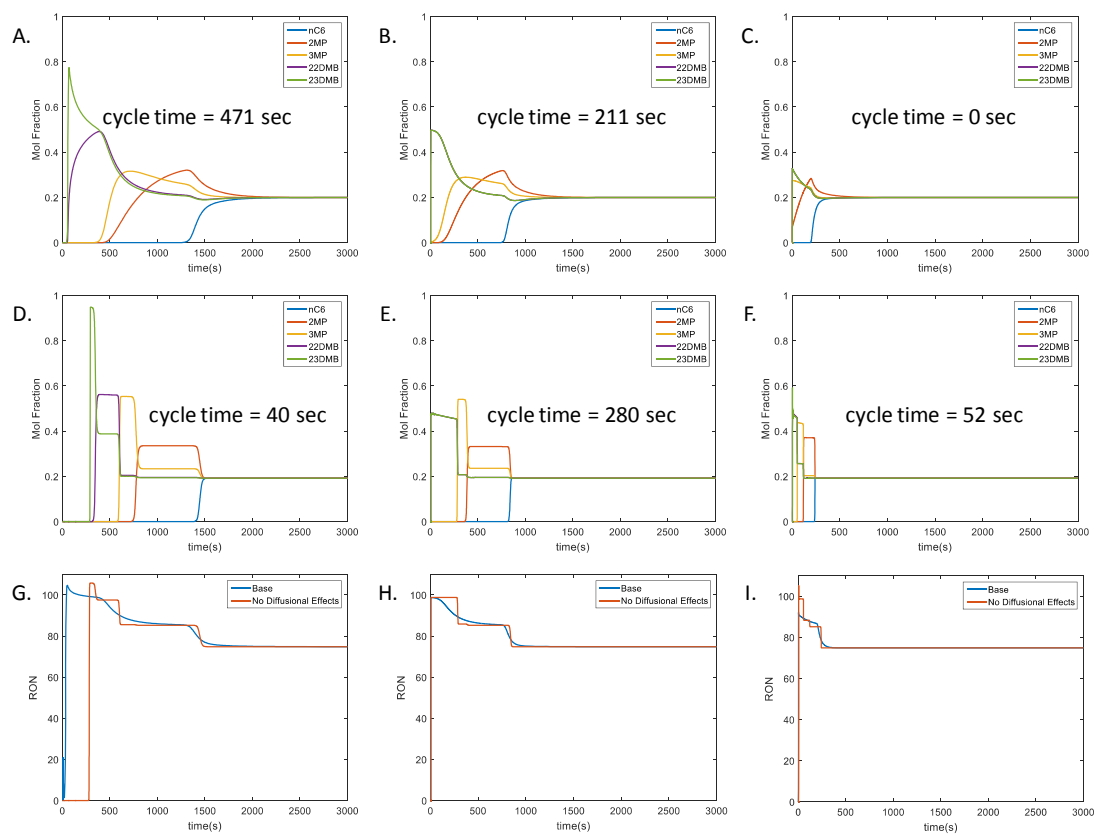


Figure S14: Comparison between DEYVUA, VICDOC, and MRE-1 for **Base Case** and **Case III**: **A.** *Base Case* breakthrough curves for DEYVUA, **B.** *Base Case* breakthrough curves for VICDOC, **C.** *Base Case* breakthrough curves for MRE-1, **D.** *Case III* breakthrough curves for DEYVUA, **E.** *Case III* breakthrough curves for VICDOC, **F.** *Case III* breakthrough curves for MRE-1, **G.** RON values for DEYVUA, **H.** RON values for VICDOC, and **I.** RON values for MRE-1.

S9. Synthesis, Activation, and Adsorption Measurements of DEYVUA

Synthesis of DEYVUA was carried out similar to the procedures outlined in the original literature which reported the structure⁸.

Synthesis of DEYVUA-Zn

A mixture of 5-(3-carboxylphenyl) nicotic acid (0.1 mmol, 0.024 g) and $\text{Zn}(\text{NO}_3)_2 \cdot 6\text{H}_2\text{O}$ (0.2 mmol, 0.065 g) in DMF (8 mL) was placed in a 6 dram vial. The vial was capped and placed into an oven at 120 °C for 24 h. The resulting colorless polyhedral crystals were washed with DMF and acetone three times, then washed with acetone three times, and then soaked in acetone before further activation.

Synthesis of DEYVUA-Cu

A mixture of 5-(3-carboxylphenyl) nicotic acid (0.1 mmol, 0.024 g) and $\text{Cu}(\text{NO}_3)_2 \cdot 2.5\text{H}_2\text{O}$ (0.2 mmol, 0.047 g) in DMF (8 mL) was placed in a 6 dram vial. The vial was capped and placed into an oven at 120 °C for 24 h. The resulting light blue polyhedral crystals were washed with DMF three times, then washed with acetone three times, and then soaked in acetone before further activation.

Activation

Prior to sorption measurements, the **DEYVUA-Zn** or **DEYVUA-Cu** sample was soaked in acetone, replacing the soaking solution three times/h for 9 h. The wet sample was transferred into a Tristar tube and evacuated at 100 °C for 18 hours in SmartVac.

3-methylpentane (3MP) Adsorption Measurements

The 3-methyl pentane (3MP) sorption isotherm was collected on a Hiden Isochema Intelligent Gravimetric Analyzer (IGA-200), equipped with a microgram balance. The isotherm was recorded using IGASwin software (v.1) that utilizes a linear driving force model (@ > 98% equilibration had been reached) and corrects all data points for the buoyancy effects. Therefore, the adsorbed mass at a given pressure was the difference of mass gain at the point relative to the evacuated sorbent mass recorded at $P = 10^{-7}$ torr ($\sim 10^{-5}$ Pascal). The sample was pre-activated overnight at 120 °C under vacuum using a Micromeritics Smart VacPrep (SVP) system before being transferred to the IGA-200 where it was activated again until no weight loss could be observed at 10^{-7} torr. The typical dry weight sample mass was 25 – 50 mg. A saturated vapor pressure of 3MP was generated by flowing a dry N_2 -stream through a thermostat vessel at 298 K. The different partial pressures for 3MP were obtained by proportional mixing of the saturated stream with dry N_2 .

S10. N₂ and 3MP Isotherms for DEYVUA

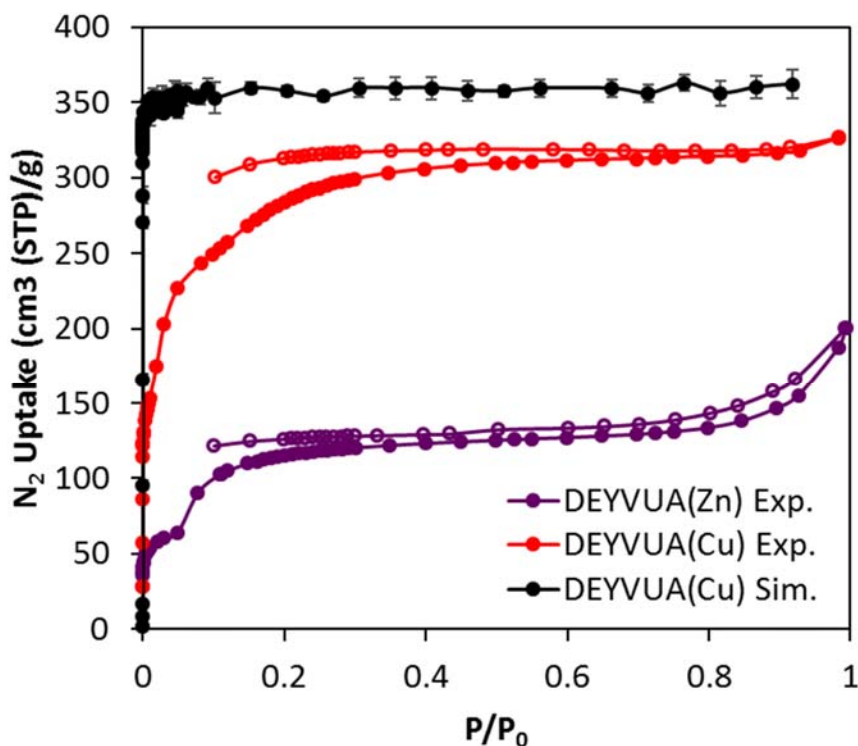


Figure S15. Comparison between experimental and simulated nitrogen isotherms for DEYVUA at 77 K. Filled circles are for adsorption branch and empty circles are for desorption branch of the isotherm.

Grand canonical Monte Carlo (GCMC) simulations were carried out to calculate the nitrogen isotherms for the copper version of DEYVUA. We note that the simulation results obtained from the zinc version of DEYVUA are very similar to the results obtained for the copper version, so we do not report them. The results, along with experimental measurements, are shown in **Figure S15**. By comparing the saturation loading of simulated and experimental nitrogen isotherms, we find that the copper version of DEYVUA shows 93% activation of the MOF sample. Given the nice activation, we expect the single component hexane isotherms to reach similar saturation loadings. Therefore, we measured the single component isotherm for 3MP at 298 K, and the results are compared with the GCMC simulation results for the same temperature in **Figure S16**.

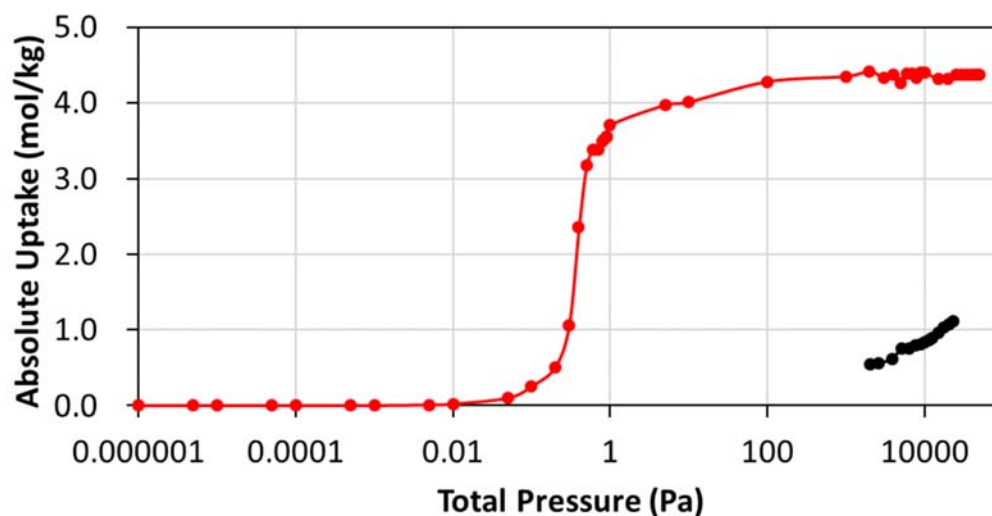


Figure S16. Comparison between experimental and simulated single component adsorption isotherm of 3-methylpentane (3MP) in DEYVUA (Cu). Solid red circles are CB-GCMC simulation results and solid black circles are from experimental measurement at 298 K.

From the figure, we can see that 3MP does not reach saturation loading even at 0.1 bar (10,000 Pa), and the uptake is only 25 % of the total possible as calculated by GCMC. This may be due to the fact that the channels in DEYVUA are small (PLD = 4.1 Å) and it may be hard for 3MP to diffuse into MOF sample and equilibrate during the period of measurement. The agreement between simulation and experiment is extremely poor, and based on the results, we did not further pursue the experimental measurement of other hexane isomers. We note that the measurements for DEYVUA are carried out at 298 K and so the diffusion of hexane isomers into the MOF crystal is slow, which may be the reason for the large difference between simulated and experimental 3MP uptake shown in **Figure S16**. However, we expect better agreement between simulation and experimental isotherms at elevated temperature (e.g., 433 K) because the increase in temperature may facilitate the diffusion of hexane isomers into the MOF pores.

S11. Analysis of Geometric Confinement in VICDOC ($\text{Fe}_2(\text{BDP})_3$)

VICDOC (Fe_2BDP_3) shows remarkable hexane isomer separation capability, which has been attributed by Long and co-workers⁹ to the presence of acute corners from triangular-shaped channels. They asserted that, in the triangular-shaped channel, *n*-hexane can fit more snugly than the branched hexane isomers, which subsequently leads to a difference in the heats of adsorption between these isomers within the channel. Using a simple geometric argument, we illustrate that the pore size of $\text{Fe}_2(\text{BDP})_3$ is not sufficiently large to accommodate hexane molecules in the corners of the channel and the sorbate molecules must be arranged single file near the center of the pore (see also Figure 5 of the manuscript and associated discussion). If we consider an equilateral triangular channel and naively take the edge length to be 13.25 Å based on the positions of the Fe atoms at the corners of $\text{Fe}_2(\text{BDP})_3$ (**Figure S17A**), we could, indeed, fit representative probe spheres near each corner of the channel. But consider an alternative, more realistic atomistic picture. We can determine a smaller, equilateral triangle that accounts for the van der Waals radii of the framework atoms based on the UFF radii. This more realistic triangle with edge length of 7.56 Å can fit only a single methyl group as represented by the TraPPE-UA model (see **Figure S17B**). The cartoon clearly shows that the corners of VICDOC's channels are not accessible to hexane isomers, but that hexane isomers are confined within ≈ 1 Å of the center of the pore. The picture is also supported by the potential energy surfaces and density maps presented in the main text.

Further evidence for single-file siting in VICDOC can be gleaned from the one-dimensional center-of-mass distribution function for *n*-hexane computed in the direction of the long axis of the triangular channels. If more than one molecule would fit in the same channel segment, then one would expect a sequence of peaks as is typical for tightly packed alkanes. As can be seen from **Figure S18**, the center-of-mass distribution does not show multiple peaks, which indicates that the adsorption of *n*-hexane in this channel is single-file.

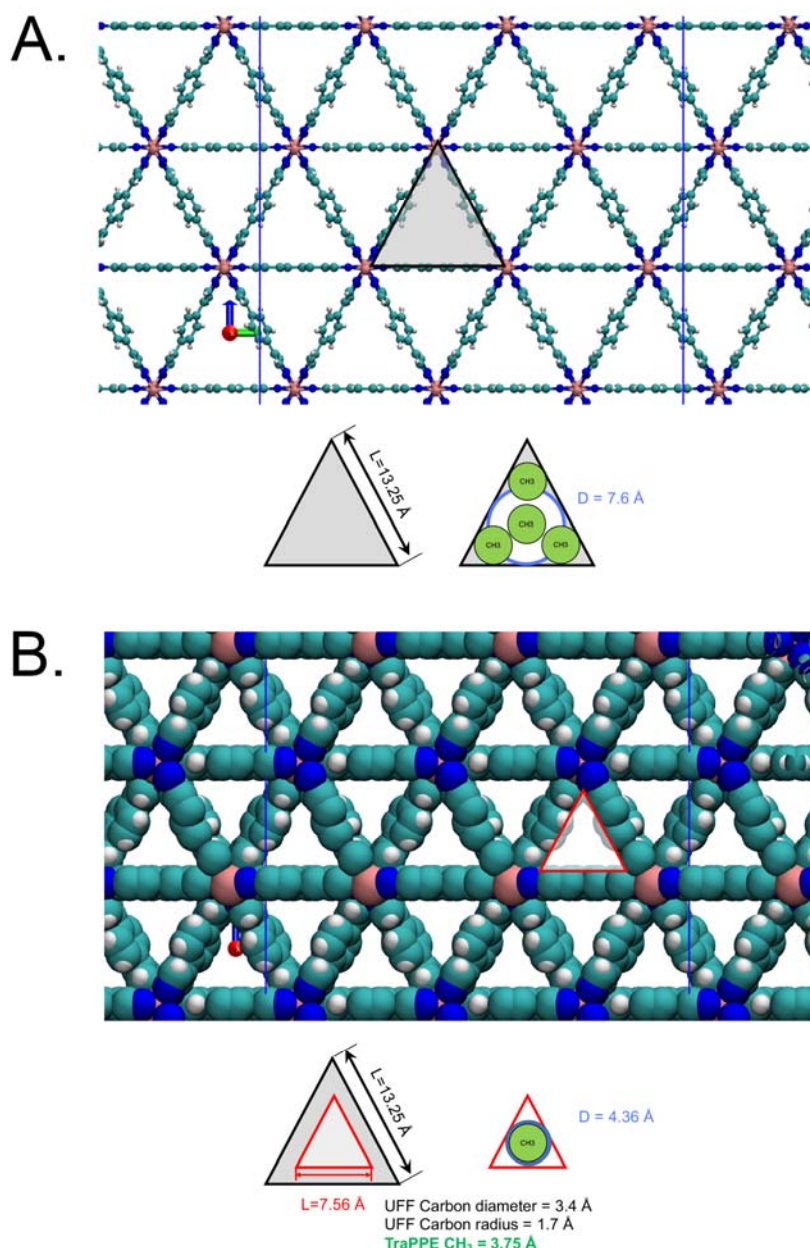


Figure S17. Visualization of the molecular structure of VICDOC: **A.** CPK representation and a cartoon of the equilateral triangle formed by connecting three Fe atoms (pink) at the nodes of the channels. The triangle can fit a circle with a diameter of 7.6 \AA and can accommodate up to 4 TraPPE-UA methyl groups; **B.** vdW representation and a cartoon of the Fe-Fe-Fe equilateral triangle (shown as black line) and a smaller equilateral triangle (shown as red line) that accounts for the pore size reduction of 1.7 \AA in all directions due to the van der Waals radius of carbon atoms forming the channel walls. This smaller triangle has an edge length of 7.56 \AA and can fit a circle with a diameter of 4.36 \AA . This channel can only accommodate a single methyl group as depicted by the cartoon in bottom right. All cartoons are drawn to scale.

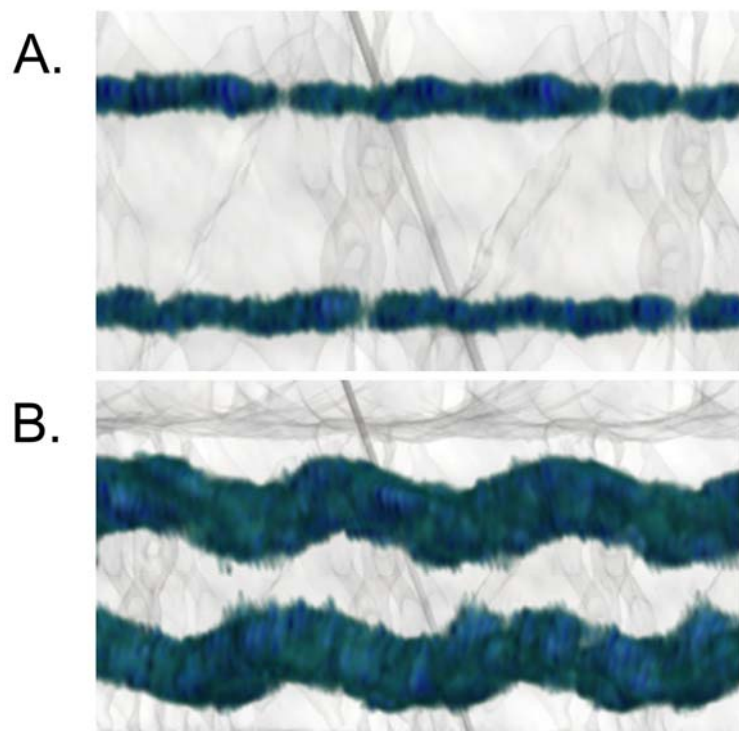


Figure S18. **A.** Center-of-mass distribution and **B.** density map of individual beads along the long axis of the VICDOC channels computed for *n*-hexane from the unary adsorption at 1 bar. **A** and **B** are drawn with the same scale, and gray shades are the MOF surface. The straight gray line that goes behind the channel is the edge of the unit cell.

S12. Analysis of Free Energy of Adsorption for Hexane Isomer Separation

We computed the Helmholtz free energy of adsorption at infinite dilution ($\Delta A_{\text{ads},i}$) of each isomer i for a selected set of CoRE MOF structures with high isomer selectivity to investigate the underlying mechanism for isomer separations. We calculated $\Delta A_{\text{ads},i}$ for hexane isomers using the Henry's law constants as calculated from the Widom particle insertion simulations:

$$\Delta A_{\text{ads},i} = -RT \ln(RT \rho_s K_{\text{H},i}) \quad \text{Eq. S3}$$

where R is the gas constant (kJ / mol K), T is the absolute temperature (K), ρ_s is the density of the framework (kg / m³), and $K_{\text{H},i}$ is the Henry's law constant of isomer i (mol / kg Pa). We can re-cast the expression in terms of the enthalpy ($\Delta H_{\text{ads},i}$) and entropy ($-T\Delta S_{\text{ads},i}$) of adsorptions as follows:

$$\Delta A_{\text{ads},i} = \Delta H_{\text{ads},i} - RT - T\Delta S_{\text{ads},i} \quad \text{Eq. S4}$$

The values of $\Delta H_{\text{ads},i}$ can be decomposed into:

$$\Delta H_{\text{ads},i} = \langle \mathcal{V}_{\text{gh},i} \rangle - \langle \mathcal{V}_{\text{h}} \rangle - \langle \mathcal{V}_{\text{g},i} \rangle + RT \quad \text{Eq. S5}$$

where $\langle \mathcal{V}_{\text{gh},i} \rangle$ is the average of the sum of the intermolecular potential energy between guest and host and the intramolecular potential energy of the guest component i and the host framework. $\langle \mathcal{V}_{\text{h}} \rangle$ is the potential energy of the host framework that is set to zero for a rigid framework, and $\langle \mathcal{V}_{\text{g},i} \rangle$ is the average intramolecular potential energy of an isolated molecule of component i , which is obtained from a separate set of simulations for each hexane isomer. The expression for $-T\Delta S_{\text{ads},i}$ can be obtained by combining Eq. S3 and S4,

$$-T\Delta S_{\text{ads},i} = -RT \ln(RT \rho_s K_{\text{H},i}) - \Delta H_{\text{ads},i} + RT \quad \text{Eq. S6}$$

To assess the relative importance of enthalpy and entropy of adsorption to the separation of n -hexane from mono-branched isomers, and of the latter from di-branched isomers, we plot the differences of $\Delta A_{\text{ads},i}$ as a function of the corresponding difference in the entropy and in the enthalpy of adsorption values for all CoRE MOFs and IZA zeolites (Figures S19 and S20) with $S_{\text{L+M}} > 100$.

The scatter plots can be interpreted as follows: i) if the data points coincide with the parity line for either $-T\Delta S_{\text{ads},i}$ or $\Delta H_{\text{ads},i}$, then the $\Delta A_{\text{ads},i}$ difference originates entirely from this thermodynamic contribution; ii) if the data points fall on the x-axis, then the corresponding thermodynamic contribution is insignificant for the difference in $\Delta A_{\text{ads},i}$. The analysis provides qualitative insight into the underlying thermodynamic factors that enable the hexane isomer separation. For example, the separation between the linear and the mono-branched isomers is due to both enthalpic and entropic contributions to the free energy of adsorption. **Figure S19a** shows that the entropic penalty for n -hexane is generally less in magnitude than for mono-branched hexane isomers. This occurs because both linear and mono-branched hexane isomers lose their degrees of freedom when they are adsorbed in the pores, but n -hexane still has sufficient degrees of freedom compared with mono-branched hexane isomers. However, the data shows that the separation between mono- and dibranched isomers in high-performing structures is almost entirely due to the difference in the enthalpy of adsorption (**Figure S19b and d**). This occurs because both mono- and di-branched hexane isomers do not

have sufficient degrees of freedom upon adsorption in tight-fitting (thus highly selective) pores. Similar trends are observed for IZA zeolites (**Figure S20**).

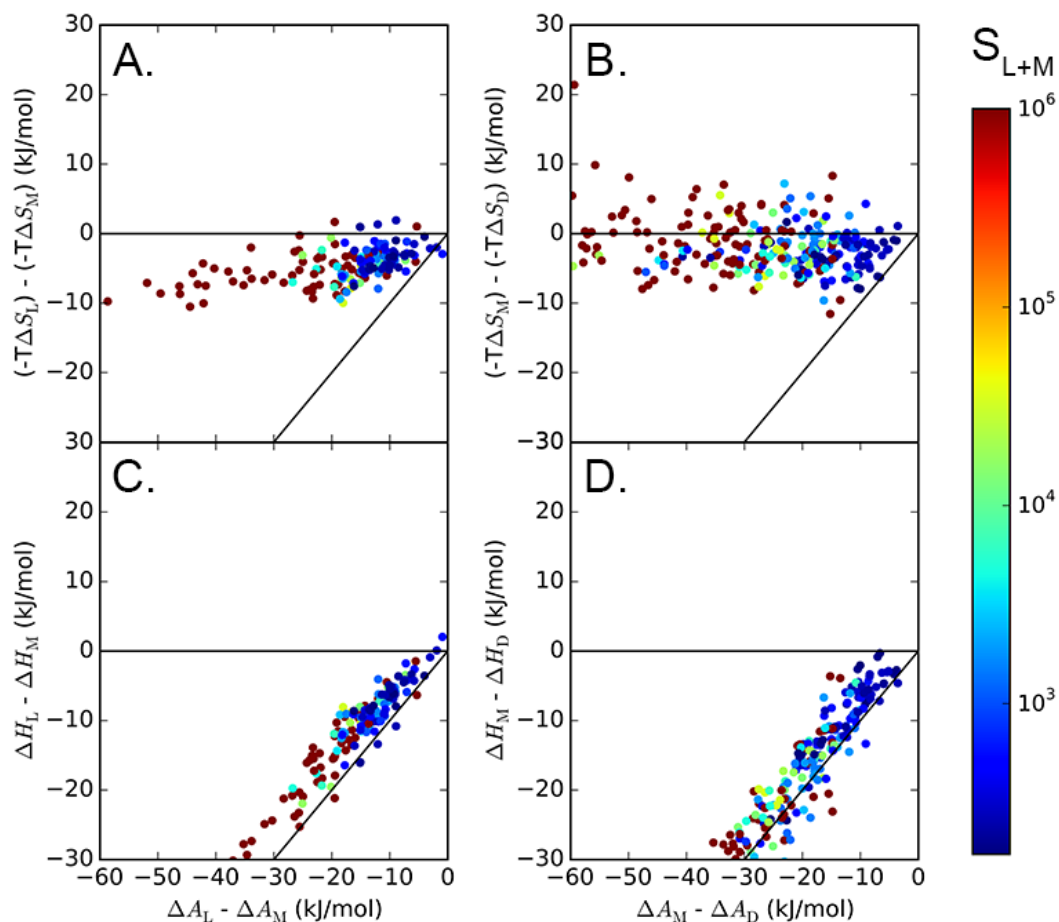


Figure S19. The difference in the Helmholtz free energy of adsorption between: **A., C.** linear (ΔA_L) vs. mono-branched hexane isomers (ΔA_M); and **B., D.** mono-branched (ΔA_M) and di-branched hexane isomers (ΔA_D). In **A** and **C**, both $\Delta A_{nC6} - \Delta A_{2MP}$ and $\Delta A_{nC6} - \Delta A_{3MP}$ values are plotted for CoRE MOF structures. Each data point corresponds to either $\Delta A_{nC6} - \Delta A_{2MP}$ or $\Delta A_{nC6} - \Delta A_{3MP}$ from a CoRE MOF with $S_{L+M} > 100$. In **B** and **D**, $\Delta A_{2MP} - \Delta A_{22DMB}$, $\Delta A_{2MP} - \Delta A_{23DMB}$, $\Delta A_{3MP} - \Delta A_{22DMB}$, and $\Delta A_{3MP} - \Delta A_{23DMB}$ values are plotted for CoRE MOF structures. Each data point corresponds to either $\Delta A_{2MP} - \Delta A_{22DMB}$, $\Delta A_{2MP} - \Delta A_{23DMB}$, $\Delta A_{3MP} - \Delta A_{22DMB}$, or $\Delta A_{3MP} - \Delta A_{23DMB}$ from a CoRE MOF with $S_{L+M} > 100$. Data points are colored based on the value of S_{L+M} . Solid black lines are the parity lines.

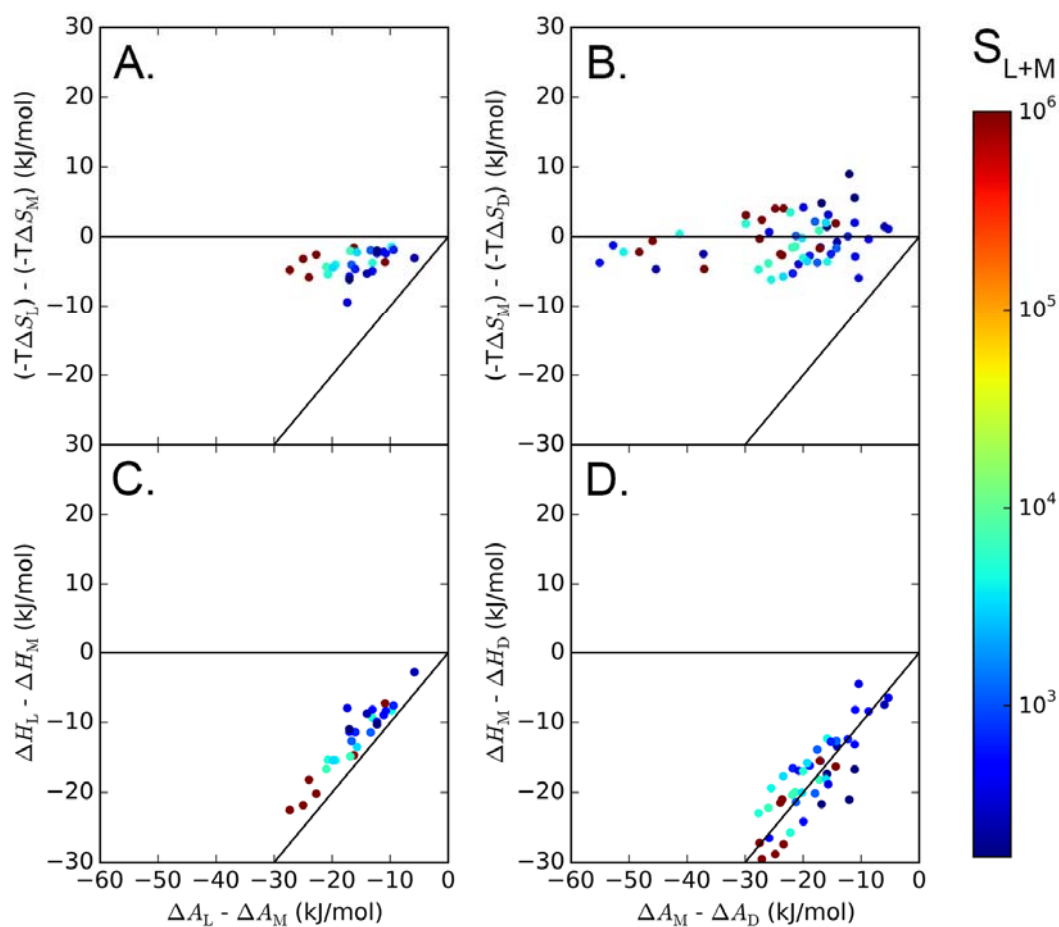


Figure S20. The difference in the Helmholtz free energy of adsorption between: **A.**, **C.** linear (ΔA_L) vs. mono-branched hexane isomers (ΔA_M), and **B.**, **D.** mono-branched (ΔA_M) and di-branched hexane isomers (ΔA_D). In **A.** and **C.**, both $\Delta A_{nC6} - \Delta A_{2MP}$ and $\Delta A_{nC6} - \Delta A_{3MP}$ values are plotted for IZA zeolites. Each data point corresponds to either $\Delta A_{nC6} - \Delta A_{2MP}$ or $\Delta A_{nC6} - \Delta A_{3MP}$ from an IZA zeolite with $S_{L+M} > 100$. In **B.** and **D.**, $\Delta A_{2MP} - \Delta A_{22DMB}$, $\Delta A_{2MP} - \Delta A_{23DMB}$, $\Delta A_{3MP} - \Delta A_{22DMB}$, and $\Delta A_{3MP} - \Delta A_{23DMB}$ values are plotted for IZA zeolites. Each data point corresponds to either $\Delta A_{2MP} - \Delta A_{22DMB}$, $\Delta A_{2MP} - \Delta A_{23DMB}$, $\Delta A_{3MP} - \Delta A_{22DMB}$, or $\Delta A_{3MP} - \Delta A_{23DMB}$ from an IZA zeolite with $S_{L+M} > 100$. Data points are colored based on the value of S_{L+M} . Solid black lines are the parity lines.

S13. DEYVUA

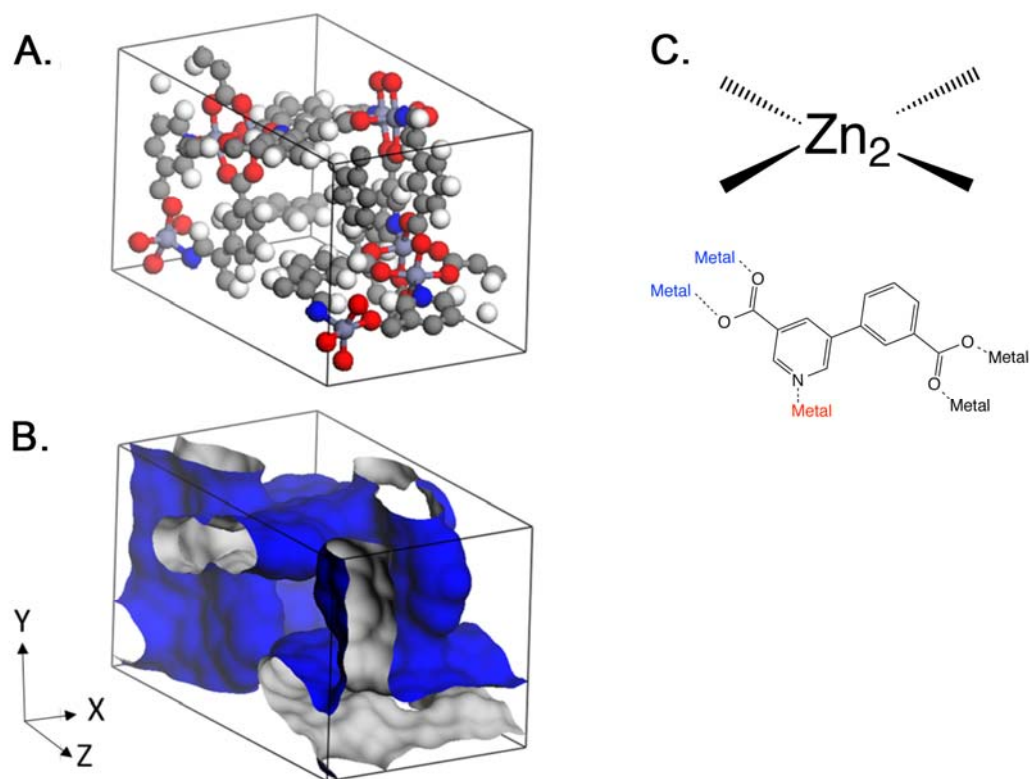
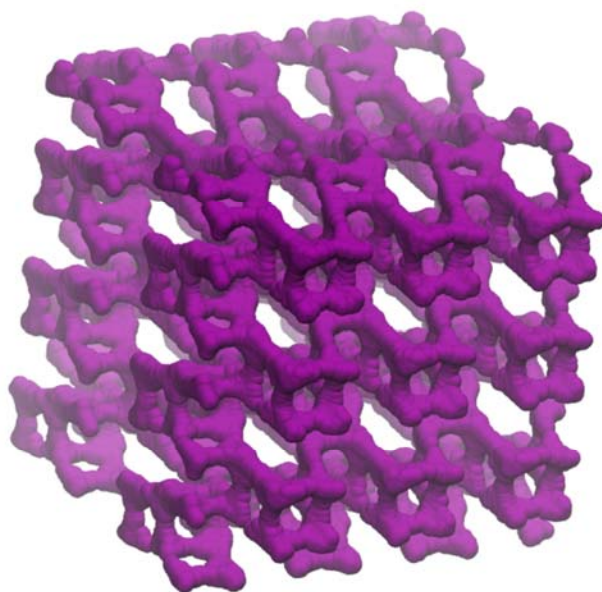


Figure S21. Structure of DEYVUA⁸: **A.** Ball-and-stick representation of the unit cell of DEYVUA. Carbon atoms are shown in black, oxygen atoms in red, zinc atoms in light purple, nitrogen atoms in blue, and hydrogen atoms in white; **B.** van der Waals surface representation of DEYVUA. Blue surface points towards the channel interior; **C.** Inorganic (Zn-paddle wheel) and organic (5-(3-carboxyphenyl) nicotinic acid (H₂dcpa)) building blocks that form DEYVUA. Organic building block connects with three different inorganic building blocks as depicted by blue, red, and black metals.

A.



B.

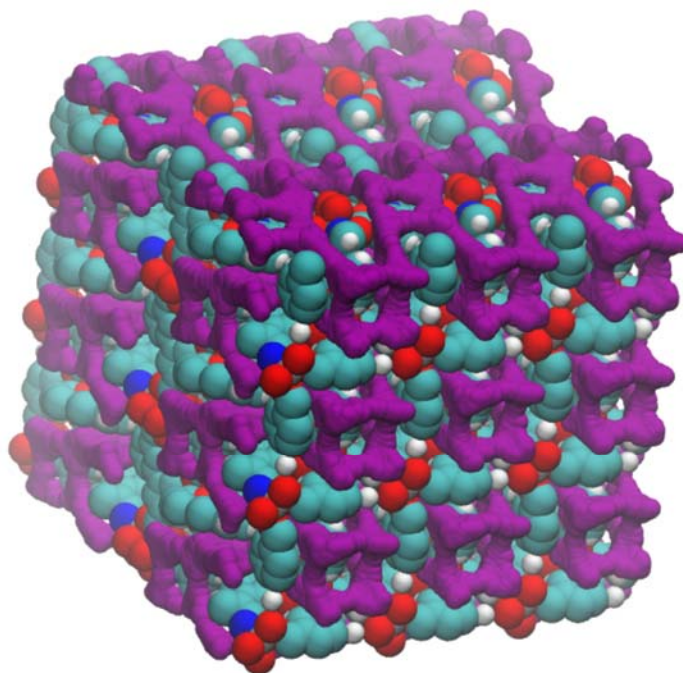


Figure S22. Representation of the pore void within DEYVUA. **A.** Illustration of the pore void within DEYVUA, viewed along $\langle 1\ 1\ 1 \rangle$ axis. The void is colored purple and the atoms of DEYVUA are removed for clarity. Pore void is created using the poreblazer software with probe size of 4.0 angstrom¹⁰; **B.** Overlap of the pore void and framework atoms of DEYVUA. DEYVUA has a 3-dimensional intersecting channel with PLD value of 4.4 angstrom, and LCD value of 5.4 angstrom.

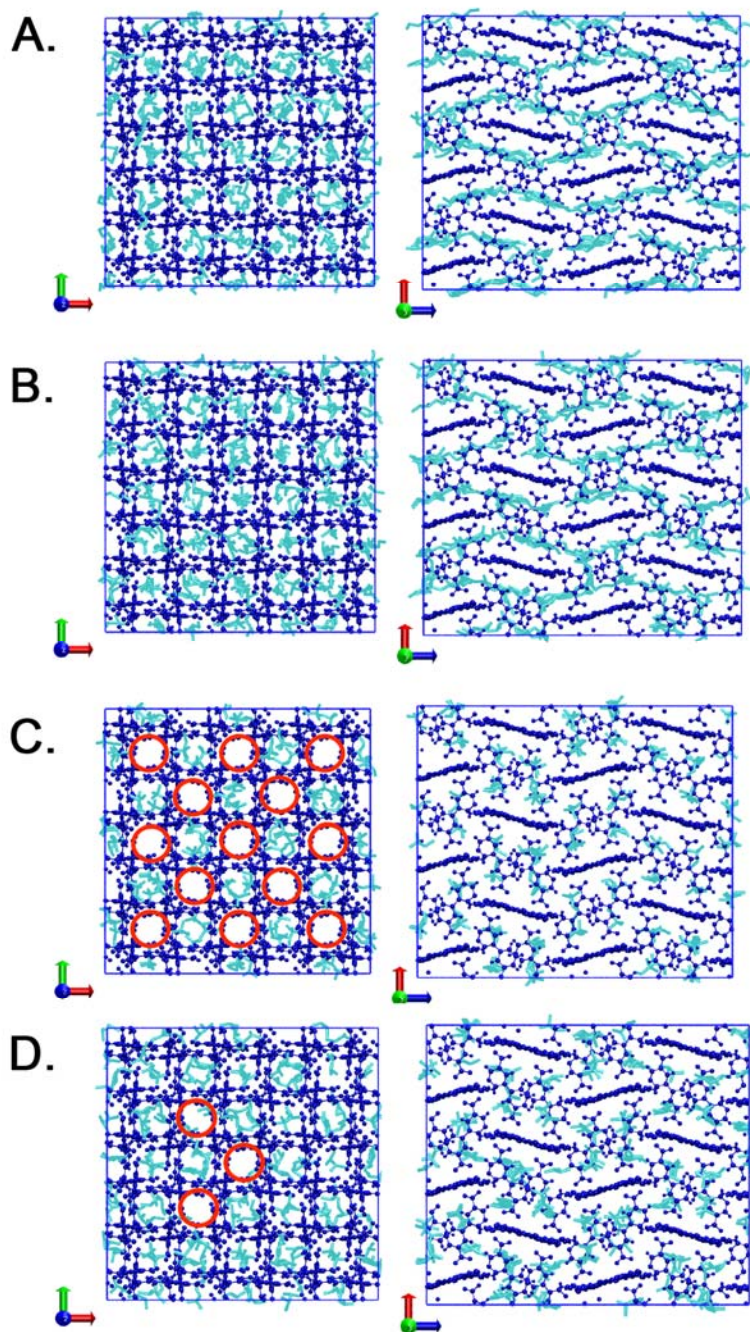


Figure S23. Snapshots of hexane isomers (cyan) during pure component GCMC simulation of DEYVUA at 1 bar and 433 K. Snapshots on left are the projections on xy-plane and snapshots on the right are the projections on xz-plane. Dark blue atoms are framework atoms for DEYVUA: **A.** nC6, **B.** 2MP, **C.** 22DMB, and **D.** 23DMB. Red circles in **C** and **D** show empty channels.

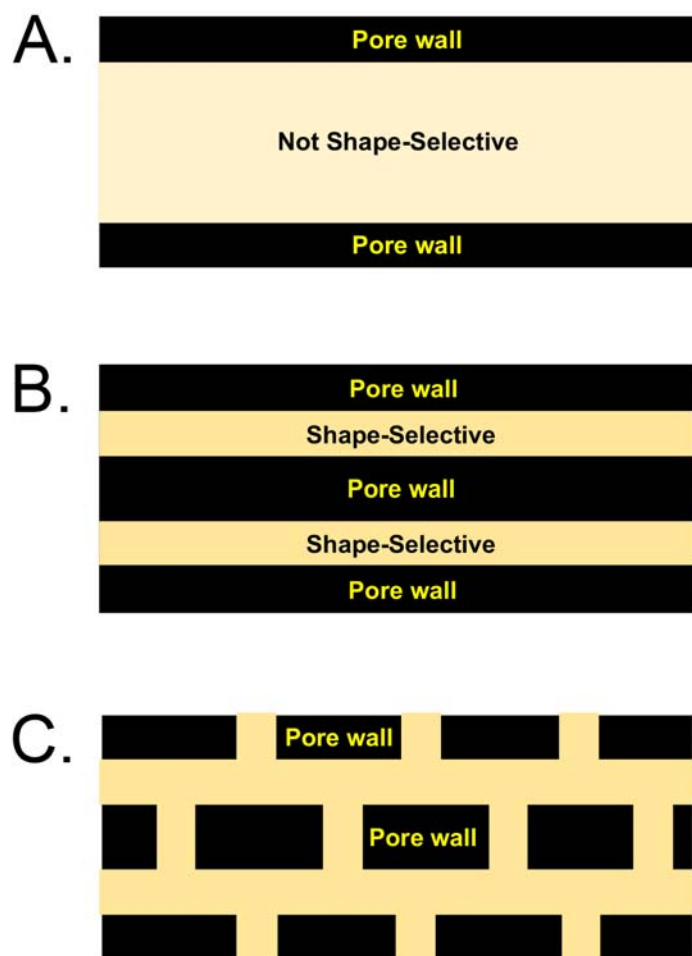


Figure S24. Illustration of the origin of shape selectivity and high capacity in DEYVUA. **A.** Large pores are not selective to hexane isomers because there is not enough interaction between the adsorbate and the pore wall; **B.** Small pores can selectively adsorb hexane isomers based on their degree of branching by providing a confinement of hexane isomers and restricting their degrees of freedom (e.g., VICDOC); **C.** Small 3-dimensional intersecting pores can provide a higher capacity than the structure with just 1-D channels (as illustrated in **B.**), because more hexane isomers can fit per volume of the material (e.g., DEYVUA).

S14. Effect of Solvent Molecule Evacuation in Adsorption Properties in VICDOC

We investigated the effect of solvent removal on the structure of VICDOC by performing a geometry optimization of the de-solvated structure to test the effect of subtle differences in pore geometry on adsorption properties, such as selectivity and capacity. This is largely motivated by the fact that many of the structures from the CoRE MOF database are de-solvated versions, i.e., solvents which can stabilize the framework were artificially removed, which can alter the adsorption properties of molecules. The calculations were carried out with the Forcite module of Materials Studio¹¹ using an algorithm that is a series of the steepest descent, Newton-Raphson, and quasi-Newton methods. The lattice parameters were fixed at the experimentally reported values during the optimization process. The bonded and non-bonded (van der Waals) interactions between the atoms were modeled using the Universal Force Field (UFF)¹². The bond stretching was modeled by a harmonic term, angle bending by a three-term Fourier cosine expansion, and torsions and inversions by cosine-Fourier expansion terms. GCMC simulations were carried out as described in the main text. Table S8 summarizes the geometric properties of the optimized and as-is structures. The effect of structural relaxation on the adsorption properties was determined by carrying out GCMC simulations on the VICDOC structure “as is” (i.e., crystal structure with solvents removed but no relaxation) and on the optimized structure. Figures S25 and S26 show that the optimized structure yields higher capacity over the entire pressure range investigated here and higher selectivity at pressures below 0.01 bar, but lower selectivity under operational conditions ($p = 1$ bar). Nevertheless, the results show that at the operating pressure of interest, the selectivity and capacity for optimized and “as-is” structure are not that different, and the adsorption characteristics of hexane isomers remain unchanged.

Table S8: Summary of geometric optimization results for solvent-free VICDOC. Gravimetric surface areas are calculated with Zeo++.

Physical Properties	VICDOC (as-is)	VICDOC (optimized)
Pore Limiting Diameter (PLD) (Å)	4.1	4.4
Largest Cavity Diameter (LCD) (Å)	4.6	4.9
Gravimetric Surface Area (GSA) (m ² /g)	499	579

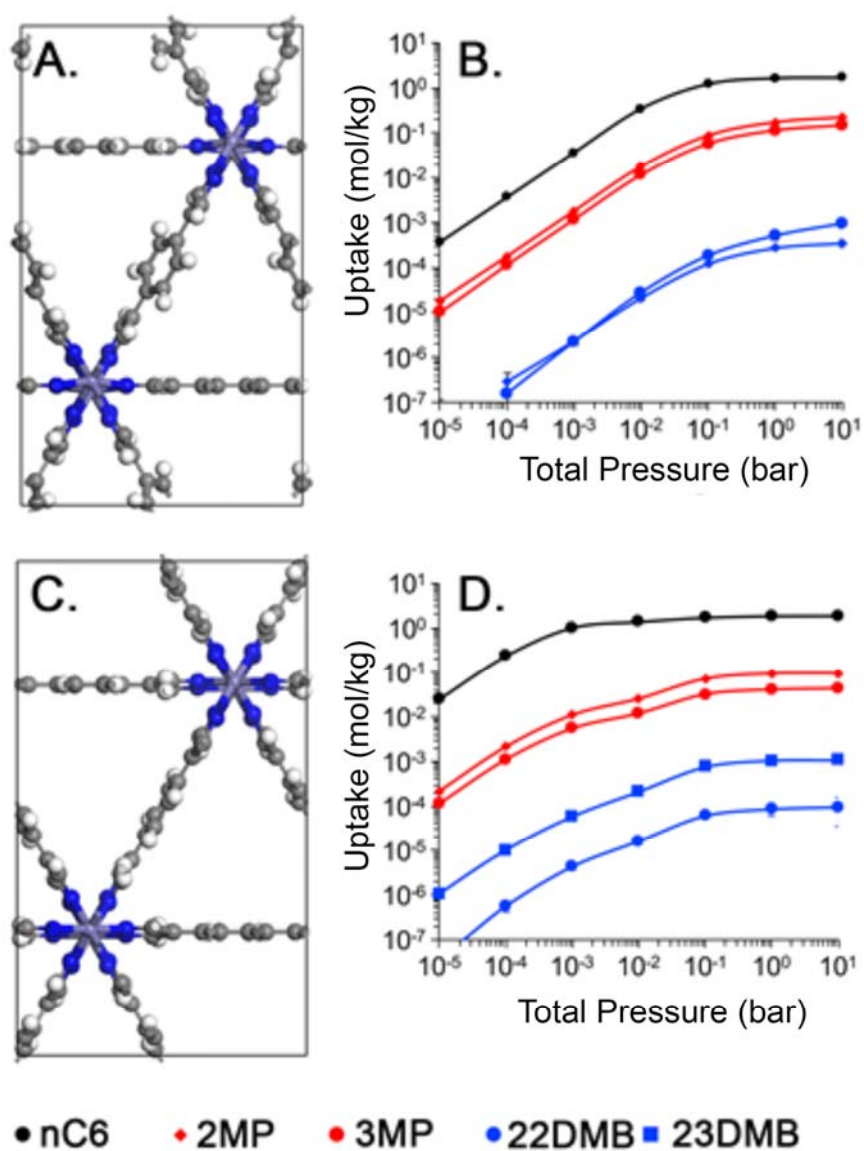


Figure S25. Atomic representation of VICDOC and corresponding 5-component mixture GCMC simulation results: **A.** Taken directly from Cambridge Structural Database; **B.** five-component mixture GCMC simulation results for **A**, **C.** optimized structure, and **D.** five-component mixture GCMC simulation results for **C**.

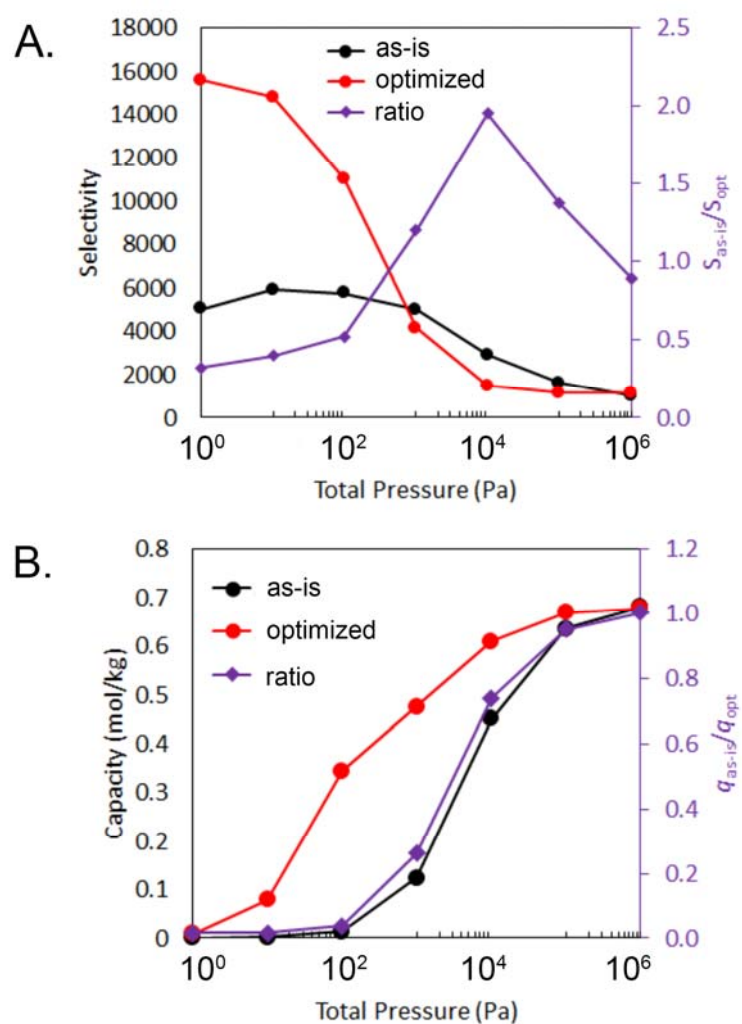


Figure S26. A. Pressure dependence of the hexane isomer selectivity; **B.** the adsorption capacity computed from the 5-component mixture adsorption simulation in VICDOC. The primary y-axes (left side) are used for black and red solid lines, and the secondary y-axes (right side) are for purple lines.

S15. Additional Potential Energy Surface and Density Plots

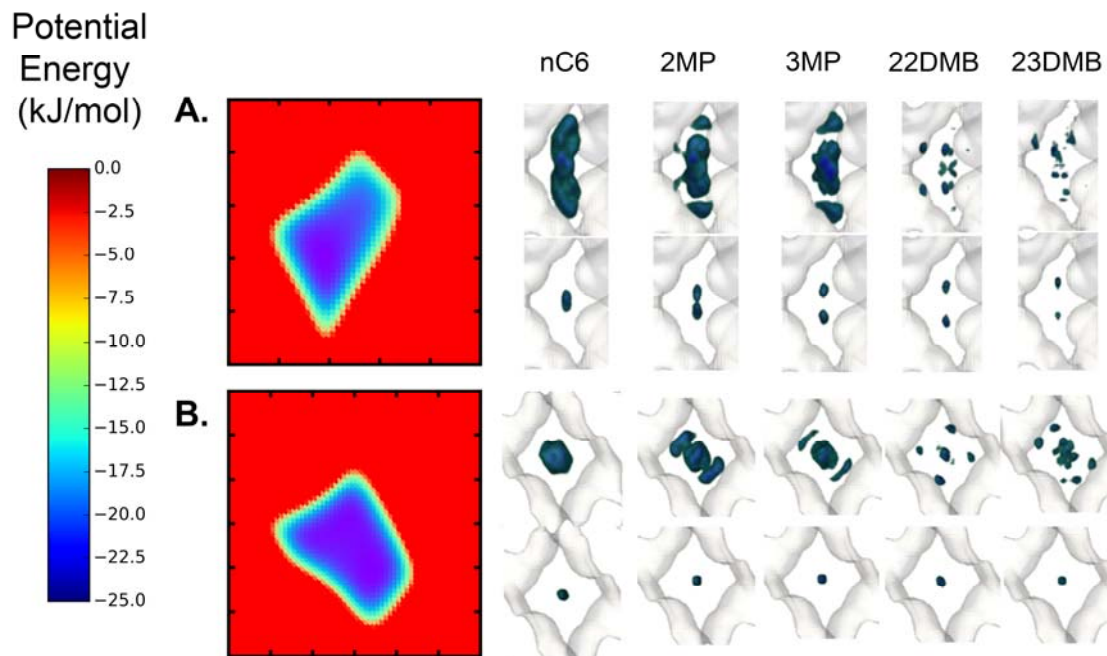


Figure S27. Visualization of selected top-performing MOFs potential energy surface (left) and density maps (right): **A.** NAPZOV; **B.** IBUDZ. The potential energy surface was calculated for a specific cross-sectional xy-plane located at a fractional z-coordinate of 0.00 for both NAPZOV and IBUDZ using the united-atom (UA) model of TraPPE-CH₃ as a probe ($\sigma = 3.75 \text{ \AA}$; $\epsilon / k_B = 98.0 \text{ K}$; $\epsilon = 0.815 \text{ kJ/mol}$). Different colors in the potential energy surface represent different values of the interaction energy (left scale bar). The clouds from the density maps are calculated from the center-of-mass of each UA bead of the hexane isomers (top row) and from the center-of-mass of each molecule (bottom row) and are projections of the entire channel length in z-direction.

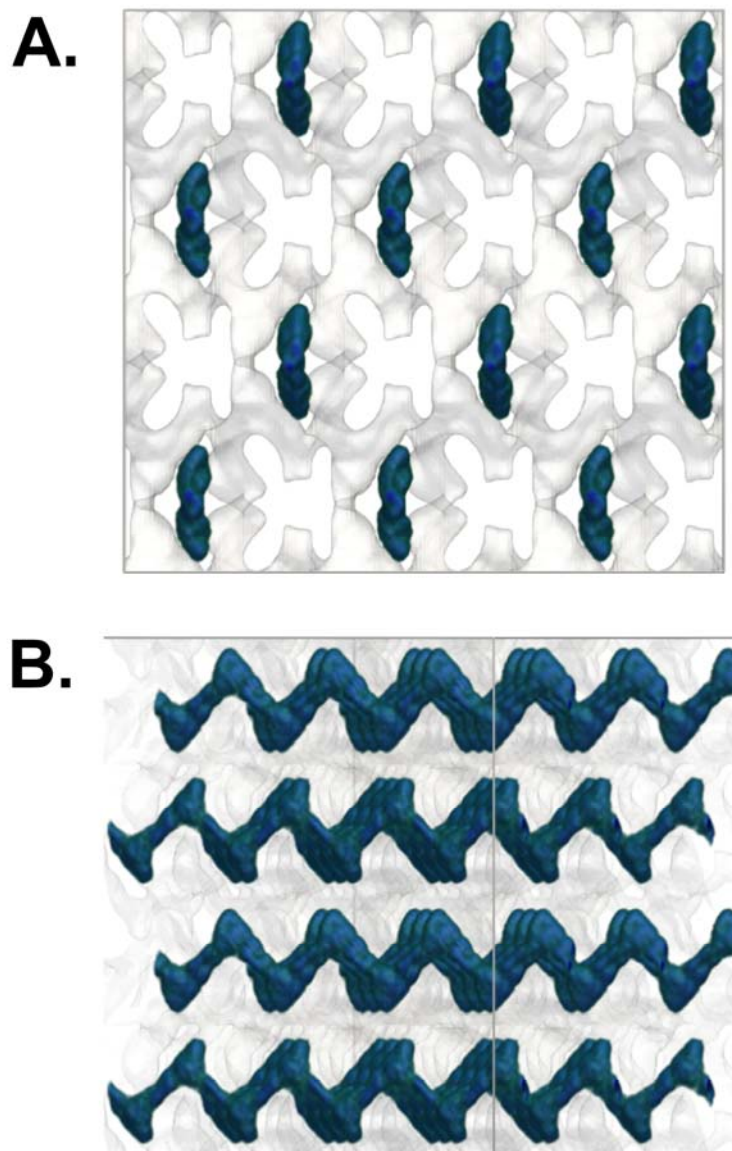


Figure S28. Visualization of density maps of *n*-hexane UA beads in NAPZOV from two different viewpoints: **A.** view from the *xy*-plane; **B.** view from the *xy*-plane with 60° rotation. The clouds from density maps are calculated as in **Figure 5** from main text.

REFERENCES

1. Linstrom, P.J.; Mallard, W. G., NIST Chemistry WebBook, NIST Standard Reference Database Number 69. (accessed September 20, 2016).
2. Li, J. R.; Kuppler, R. J.; Zhou, H. C., Selective gas adsorption and separation in metal-organic frameworks. *Chem Soc Rev* **2009**, *38*, 1477-1504.
3. Ghosh, P.; Hickey, K. J.; Jaffe, S. B., Development of a detailed gasoline composition-based octane model. *Ind Eng Chem Res* **2006**, *45*, 337-345.
4. Myers, A. L.; Praunitz, J. M., Thermodynamics of Mixed-Gas Adsorption. *AIChE J* **1965**, *11*, 121-127.
5. Vandenbroeke, L. J. P.; Krishna, R., Experimental-Verification of the Maxwell-Stefan Theory for Micropore Diffusion. *Chem Eng Sci* **1995**, *50*, 2507-2522.
6. Glueckauf, E., Theory of Chromatography. Part 10. Formulae for diffusion into spheres and their application to chromatography. *Transactions of the Faraday Society* **1955**, *51*, 1540-1551.
7. Dubbeldam, D.; Krishna, R.; Calero, S.; Yazaydin, A. O., Computer-Assisted Screening of Ordered Crystalline Nanoporous Adsorbents for Separation of Alkane Isomers. *Angew Chem Int Edit* **2012**, *51*, 11867-11871.
8. Liu, B.; Li, Y. P.; Hou, L.; Yang, G. P.; Wang, Y. Y.; Shi, Q. Z., Dynamic Zn-based metal-organic framework: stepwise adsorption, hysteretic desorption and selective carbon dioxide uptake. *J Mater Chem A* **2013**, *1*, 6535-6538.
9. Herm, Z. R.; Wiers, B. M.; Mason, J. A.; van Baten, J. M.; Hudson, M. R.; Zajdel, P.; Brown, C. M.; Masciocchi, N.; Krishna, R.; Long, J. R., Separation of Hexane Isomers in a Metal-Organic Framework with Triangular Channels. *Science* **2013**, *340*, 960-964.
10. Sarkisov, L.; Harrison, A., Computational structure characterisation tools in application to ordered and disordered porous materials. *Mol Simul* **2011**, *37*, 1248-1257.
11. *Materials Studio*, Accelrys Software Inc. San Diego, CA 92121, USA: 2001 - 2011
12. Rappe, A. K.; Casewit, C. J.; Colwell, K. S.; Goddard, W. A.; Skiff, W. M., UFF, a Full Periodic-Table Force-Field for Molecular Mechanics and Molecular-Dynamics Simulations. *J Am Chem Soc* **1992**, *114*, 10024-10035.